Numerical modeling of microplastic interaction with fine sediment under estuarine conditions

G. Shiravani [a,*], D. Oberrecht [a], L. Roscher [c], S. Kernchen [d], M. Halbach [b], M. Gerriets [b], B.M. Scholz-Böttcher [b], G. Gerdts [c], T.H. Badewien [b], A. Wurpts [a]

[a] *Lower Saxony Water Management, Coastal Protection and Nature Conservation Agency (NLWKN), D-26506, Norden, Germany*
[b] *Institute for Chemistry and Biology of the Marine Environment (ICBM), Carl von Ossietzky University of Oldenburg, D-26129, Oldenburg, Germany*
[c] *Alfred Wegener Institute, Helmholtz Centre for Polar and Marine Research, D-27483, Helgoland, Germany*
[d] *University of Bayreuth, Department of Atmospheric Chemistry, 95440, Bayreuth, Germany*

ARTICLE INFO

ABSTRACT

Microplastic (MP) pollution is an important challenge for human life which has consequently affected the natural system of other organisms. Mismanagement and also careless handling of plastics in daily life has led to an accelerating contamination of air, water and soil compartments with MP. Under estuarine conditions, interactions with suspended particulate matter (SPM) like fine sediment in the water column play an important role on the fate of MP. Further studies to better understand the corresponding transport and accumulation mechanisms are required. This paper aims at providing a new modeling approach improving the MP settling velocity formulation based on higher suspended fine sediment concentrations, as i.e. existent in estuarine turbidity zones (ETZ). The capability of the suggested approach is examined through the modeling of released MP transport in water and their interactions with fine sediment (cohesive sediment/fluid mud). The model results suggest higher concentrations of MP in ETZ, both in the water column as well as the bed sediment, which is also supported by measurements. The key process in the modeling approach is the integration of small MP particles into estuarine fine sediment aggregates. This is realized by means of a threshold sediment concentration, above which the effective MP settling velocity increasingly approaches that of the sediment aggregates. The model results are in good agreement with measured MP mass concentrations. Moreover, the model results also show that lighter small MP particles can easier escape the ETZ towards the open sea.

1. Introduction

Due to the outstanding properties of plastics like lightness, durability, corrosion resistance and economical effectiveness, their application and hence mass production in the industrial as well as daily life has exponentially increased (Da Costa et al., 2020). As a result, plastics are an omnipresent part in our work and daily life. In 2019 the global plastic production has been increased to almost 368 million tons (PlasticsEurope, 2020) compared to 1.5 million tons in 1950 (PlasticsEurope, 2009) and is expected to reach 25 billion tons by 2050 (Geyer et al., 2017). The numerous adverse effects of the released/mismanaged plastics in nature on micro/macro-organisms have been reported and documented during the last decade (e.g. Koelmans et al., 2019). However, the understanding of transport mechanisms and corresponding physics from detection to modeling are in their infancy. As a simple instance, there is not a

commonly accepted definition for MP with respect to its size, which can lead to a spectrum of measured/modelled result interpretation. An international research workshop on the occurrence, effects, and fate of microplastic marine debris proposed 5 mm as the upper size limit for MP (Arthur et al., 2009), and usually 1 μm is considered in literature as the lower limit (Allen et al., 2022).

MP is classified into two groups with respect to its origin; primary MP is manufactured in sizes < 5 mm (Laskar and Kumar, 2019) and mostly applied to cosmetic/textile products (Rugerro et al., 2020) or is available for industrial use as pre-produced pellets. Secondary MP results from macro-/meso-plastics through fragmentation (chemical), UV-induced photo-degradation (solar) (Andrady, 2022), biodegradation (microbial) (Miri et al., 2022) and abrasion (mechanical) (Song et al., 2017). With respect to this classification, it can be concluded that surface runoff, municipal as well as industrial waste water treatment plants
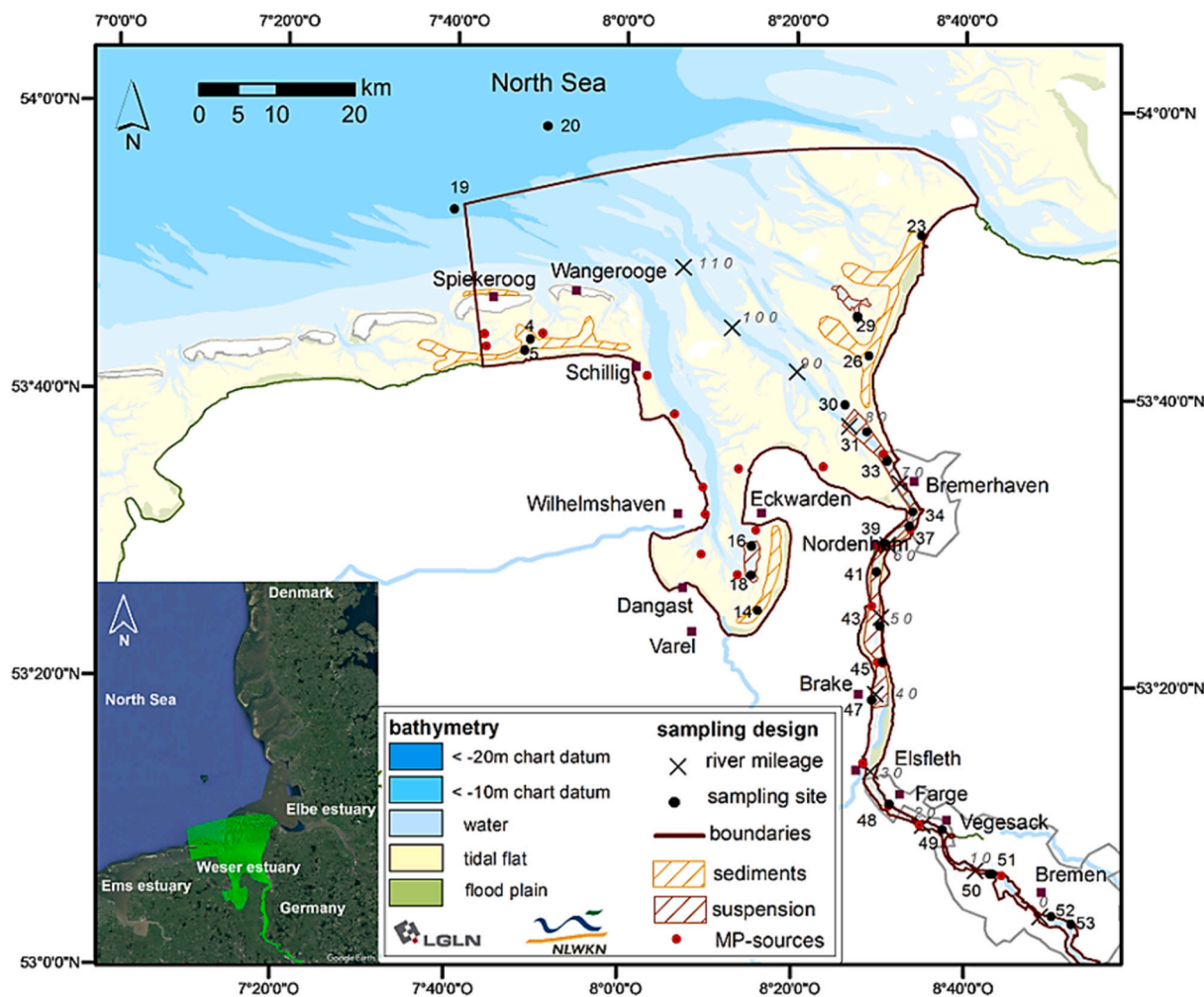

Fig. 1. Study area and model domain (green mesh in lower left inlay), sampling locations for water, sediment suspension and soil sediment (black dots), effluent of WWTPs into the receiving water as MP point sources (red dots) and cities (purple squares). (For interpretation of the references to colours in this figure, the reader is referred to the web version of this article.)

(WWTPs) are relevant entry pathways for MP into rivers/tributaries (Kay et al., 2018). MP contamination loads in rivers are commonly categorized based on the types of input as point (e.g. WWTP) and diffusive sources (e.g. MP from atmospheric deposition (Kernchen et al., 2022) or surface runoff).

Rivers as the recipients and pathways of MP contamination loads are supposed to play an important role in the MP-transport, distribution and accumulation. It is estimated that on a yearly basis between 1.15 and 2.41 million tons of MP enter into the open oceans through rivers (Lebreton et al., 2017). Moreover, the presence of diverse habitats of micro/macro organisms in rivers and their direct exposure to MP (McCormick et al., 2020; Green et al., 2017), which have a high capacity in adsorption of other toxic pollutants (Turner and Holmes, 2015), pronounces the importance of more investigations on MP-transport in rivers. Above all, since drinking water that is indirectly provided by rivers (Jung et al., 2022), as well as food resources (e.g. fish) (Wootton et al., 2021) emphasize the necessity of these investigations. So far, most of the available research about MP-pollution has been focused on open oceans and alluvial river systems (e.g. Auta et al., 2017). Accordingly, the MP-transport in tidal rivers and estuaries needs further investigation (e.g. Song et al., 2022).

The research project PLAWES (Microplastic contamination in the Weser-Wadden Sea — National Park Model System: an Ecosystem-Wide Approach, 2017–2021) was funded by the German Federal Ministry of Education and Research to support the investigation of analytical MP-measurement methods as well as the development of numerical tools and other, biota- and social science related investigations. PLAWES aimed to improve the understanding of the basic mechanisms associated with MP-transport for the whole Weser River catchment down to the German Wadden Sea. The methods and approaches (analytical, models) that were developed in PLAWES are considered to be transferable to other river catchments and estuaries as well.

The presented study describes a new numerical estuarine MP-transport model with focus on the intense physical interaction between MP and the estuarine cohesive fine sediment dynamics such as inclusion of MP items in fine sediment aggregation and flocculation processes by means of adhesion and cohesion. The MP-transport model is coupled with a three dimensional hydro-/morphodynamic numerical model. The paper covers the specific implementation and the application of the model system and shows a first comparison with observed MP mass concentrations. The approach considers the interaction of MP and estuarine cohesive fine sediments with respect to processes like flocculation, aggregation and hindered settling.

Due to the lack of sufficient measured data the model results should so far be seen as a proof of general feasibility rather than a full real-world reproduction. Also the enormous gain of process understanding with respect to the complex transport patterns in estuarine systems becomes clear. This research is distinguished by the combination of measurements/analyses and numerical modeling and therefore provides a tool for further investigations and system understanding.

Table 1

The applied data for model boundary and initial condition.

Parameter	Application, location	Data type	Source
Bathymetry	Boundary and initial condition, model domain	Area measured	Digital Elevation Model (DGM-W 2015) of Federal Waterways and Shipping Administration (WSV)
Upstream discharge	Boundary condition, upstream boundary Intschede and tributaries	time-series	WSV
Salinity	Boundary condition, upstream boundary Intschede, seaside boundary Leuchtturm Alte Weser	time-series	WSV
Temperature	Boundary condition, seaside boundary, Leuchtturm Alte Weser	time-series	WSV
Wind speed	Boundary condition of the model surface	area modelled	the German Weather Service (DWD)-ICON Model
Wind direction	Boundary condition of the model surface	area modelled	DWD-ICON Model
Air pressure	Boundary condition of the model surface	area modelled	DWD-ICON Model
Light irradiance	Surface boundary condition	area modelled	DWD measurements
Bed composition	Initial condition, model domain	area measured	WSV, AufMod (Valerius et al., 2013)
Sediment concentration	Boundary condition, upstream boundary Intschede	time-series	WSV
MP-particle concentration	Boundary condition, upstream boundary Weser-Weir and seaside boundary	point measurement	Roscher et al. (2021)
MP-mass concentration	initial condition, model domain	point measurement	Halbach & Scholz-Boettcher (this paper, but will be published elsewhere)
MP-atmospheric flux (particle concentration)	Boundary condition, model domain	point measurement	Kernchen et al. (2022)
MP-particle concentration	Boundary condition, WWTPs effluent	point measurements	Mintenig et al. (2017)
WWTPs effluents and capacity	Boundary condition, WWTPs effluent	time series, single values	Lower Saxony Water Management, Coastal Protection and Nature Conservation Agency (NLWKN)-Lage Bericht (2017), hanseWasser Bremen GmbH, Bremen's Senator for Environment, Construction, Transportation-Lage Bericht 2017

As the applied assessment methods and resulting MP item concentrations in the Weser Wadden-Sea transitional system were already presented in Roscher et al., 2021, the present study focusses on the numerical simulation results. The model approach consists of a fully coupled hydro-morphodynamic estuarine model which drives a microplastic transport model. The implemented approaches to consider the MP-fine sediment interaction and its contribution to the overall MP transport are discussed. The modelled time frame covers a period around April 2018, when a PLAWES measuring campaign took place. Calibrated and validated model results for this time window (01.04.2018–30.04.2018) are presented.

With respect to the PLAWES-project it should be noted, that the model presented here is only one part of a larger model chain which covers the whole Weser catchment including land use, runoff calculations and their MP contribution (Brandes et al., 2020). The model shown here covers the tidal part of the Weser River and the adjacent parts of the German Wadden Sea. The model chain though can be applied to virtually any catchment and estuary.

2. Material and methods

2.1. Study area

The study area is located in northwestern Germany where the River Weser discharges into the southern North Sea (Fig. 1). The open boundaries of the model domain connect it to the open sea in the North and to the upstream part of the River Weser in the South, where the freshwater discharge from the non-tidal part of the catchment is applied. Minor tributaries are connected at Vegesack, Brake and Bremerhaven. The tidal part of the Weser River stretches about 120 km between the tidal weir in Bremen and the North Sea. The averaged maximum freshwater discharge by the Intschede gage for the time span of 1941–2021 is 1201 (m^3/s), the averaged discharge 314 (m^3/s) and the averaged minimum discharge 121 (m^3/s) (https://www.fgg-weser.de/).

26 sampling stations along the Weser River as well as in the North Sea were selected based on the required measurements for the calibration and validation of the numerical model as well as inputs for open boundary conditions from the North Sea (Fig. 1). The point sources of MP in this model include 24 WWTP along the sampled Weser River section (Fig. 1).

The Weser estuary can be classified as partially stratified. This means, that a distinct large scale baroclinic circulation is superimposed on the cyclic tidal flow. As a result the estuary has a pronounced estuarine turbidity zone (ETZ) with an estuarine turbidity maximum that stretches between Brake and Bremerhaven (Fig. 1). Upstream of Brake the river can be considered fully mixed, i.e. no vertical salinity gradient exists. Further density differences result from partially high fine sediment concentrations in the ETZ, also fluid mud can temporarily be observed there.

2.2. Data for model application

For the Weser model application within the PLAWES project the following data in Table 1 were used for bathymetry, bottom composition, open boundary conditions, sources and calibration/validation. The boundary conditions at the open North Sea boundary for the hydrodynamic module were calculated by an overarching large scale model cascade as described in Knaack et al. (2006). This cascade is driven by tidal constituents (astronomic forcing) at the North Atlantic boundary as well as meteorological forcing (ICON-model, Table 1).

2.3. Modeling approach and 3D-Model setup

The 3D-model consists of three modules: a) hydrodynamics, b) morphodynamics and c) MP-transport module. The first two modules are set up using open source Delft3D-FLOW and the latter is
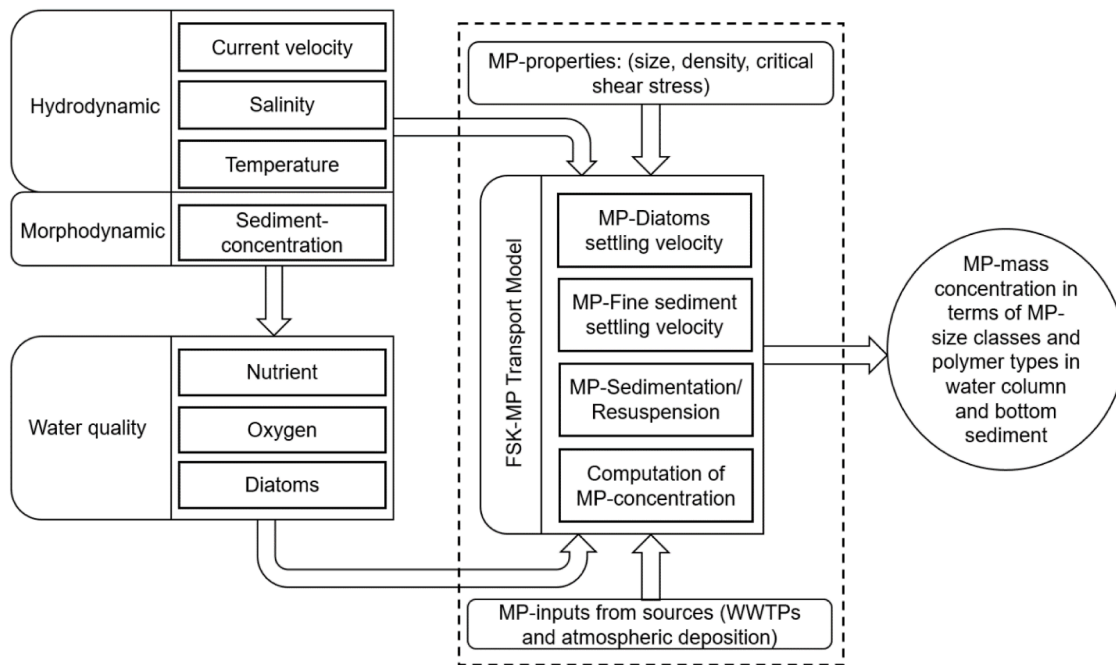
Fig. 2. Model-concept of the MP-Transport Model (FSK-MPTM).

implemented as new subroutine in the framework of D-Water Quality (DELWAQ). The numerical model code of Delft3D-Flow applied here for the hydrodynamic and morphodynamic processes is extended after Oberrecht (2021). The extension considers fluid mud dynamics and formation by including rheological behavior of high concentrated cohesive fines suspension as well as rheologically induced turbulence damping in the water column. The extended approach provides a substantial improvement of the results for the estuarine turbidity zone (ETZ). For now waves are not considered within the model approach, but a coupling with a spectral wave model basically exists.

The implementation of the 3D-module for MP-transport (FSK-MPTM) is illustrated by the conceptual sketch in Fig. 2. The model consists of three modules: (i) the hydro-/morphodynamic, (ii) water quality, and (iii) MP transport model. At the first the hydro-/morpho-dynamic parameters (current velocity, salinity, temperature, and sediment concentration) are computed using the applied model for hydro-/morphodynamic and the results are written in the form of communication data to couple with the other two parts (WAQ, FSK-MPTM), that are run as a postprocessor. Basically every suitable hydro-morphodynamic model solution (e.g. Delft3D-FLOW, TELEMAC, MIKE 21 or SCHISM) could be used to drive the latter two.

In the FSK-MPTM module, MP-properties (size, polymer density, critical shear stress for erosion and sedimentation) are input parameters which have to be set by the user.

MP-inputs as boundary conditions can be specified as point or diffusive MP sources at the corresponding positions of river/estuary. The location for point sources is defined based on the position coordinates of effluents into the river on model boundary (as depth averaged loads or separately per vertical layers). Diffusive sources are defined as fluxes through the river surface, where wind direction and speed determine the transport length from the boundary and consequently the flux surface in the model domain. In this study, MP from WWTPs and atmospheric deposition are considered. However, more complex MP modeling would require to include additional important MP-sources like i.e. tire wear and tributary inflows. The model approach can in the future include such MP-sources, which is beyond this study due to a lack of respective data.

The settling velocities of MP-particles strongly determine the transport process. Therefore, the settling velocities consider several MP-specific properties (polymer density, particle size) as well as intensive interaction with other sediment- (flocculation, aggregation, hindered settling) and microalgae (biofouling) specific processes. Since these processes strongly vary in space and time, also the resulting settling velocities vary.

The effect of biofouling on the MP-settling velocity is especially important for MP lighter than water ($\rho_{MP} < \rho_w$) like PP and PE and was reported in literature through lab experiments (Fazey et al. 2016) and field campaign (Kaiser et al., 2017). The methodology for simulation of the biofouling thickness proposed by Kooi et al. (2017) was adopted. Instead of the empirical equations for water temperature, salinity and microalgae concentration from Kooi et al. (2017) here, the modelled values from the module chain shown in Fig. 2 at each time step are used.

The approach for MP - fine sediment interaction considers different settling velocities. Depending on the local fine sediment concentration, the MP particles are considered either inert or as part of the estuarine flocculation process with transition states in between (Fig. 5).

Sedimentation and resuspension of MP into/from the bed is estimated by comparison of the computed current shear stresses in the hydro-/morphodynamic model with the critical shear stresses for sedimentation and resuspension as proposed by Waldschläger & Schüttrumpf (2019) for sandy sediments and a modified approach after Wu et al. (2018) for mixed sediments. The sedimented or resuspended MP are considered as the sinks and sources in the transport equations, respectively.

2.3.1. Hydrodynamic module

The 3D hydrodynamic module is based on a 2D-Model of Hartsuiker (2003) and Knaak et al. (2006) for the Weser estuary, which was extended into the three-dimensional domain. The model solves the three dimensional Reynolds averaged Navier Stokes equations (RANS) equations. Turbulence closure is achieved by means of a turbulent kinetic energy formulation (k-l model) considering baroclinic processes (Oberrecht, 2021). The model provides a robust scheme for tidal wetting and drying of computational cells by considering the minimum threshold depth of 10 cm. Mass conservation for the algorithm is documented in Deltares (2021a). This is a relevant feature for applications including Wadden Sea areas.

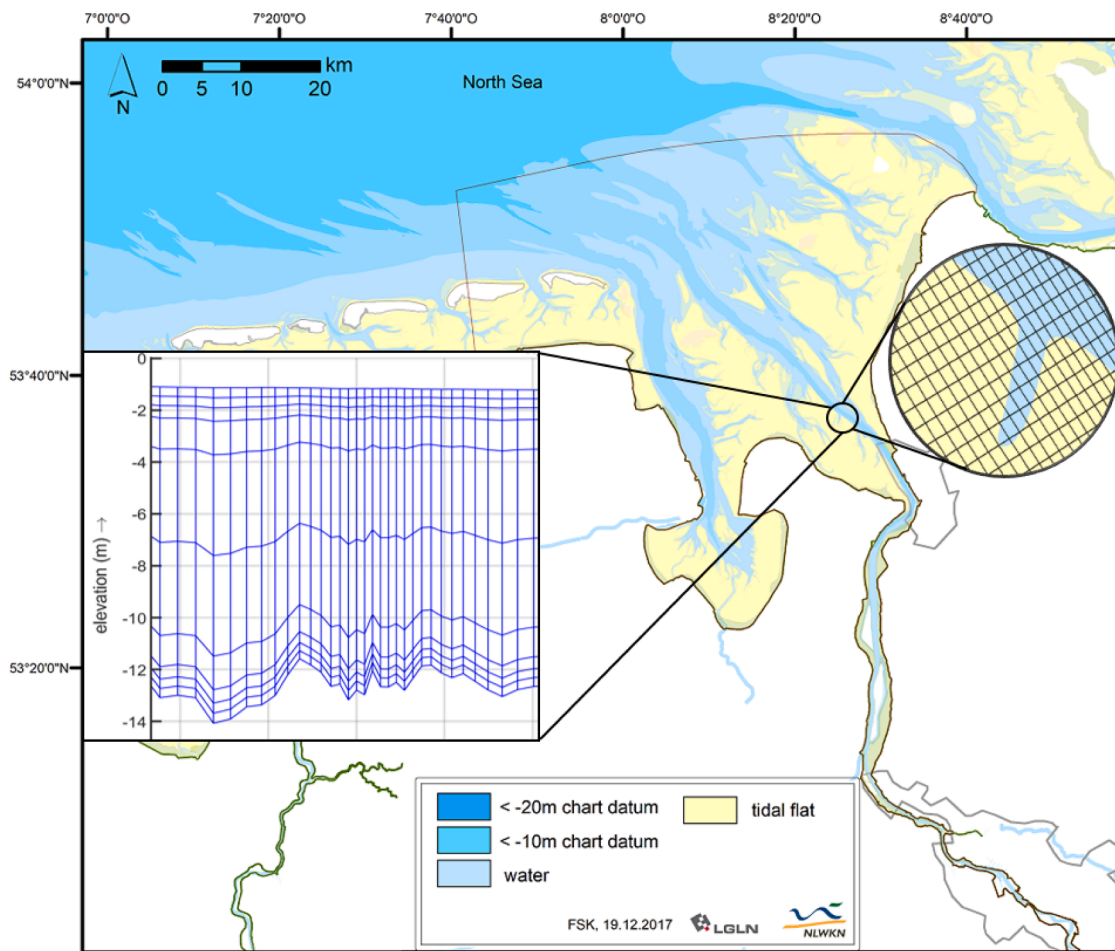The model is forced by means of the tidal water elevation changes at

Fig. 3. 3D hydrodynamic grid, left: the vertical direction (water column) and right: the water surface. (For interpretation of the references to colours in this figure, the reader is referred to the web version of this article.)

the open boundary as well as wind generated stresses on the water surface. Moreover, the time series of the river discharge at the most downstream measuring station Intschede ($52°$ $57'$ $51.048''$N, $9°$ $7'$ $32.644''$E) from the Federal Waterways and Shipping Administration (WSV) is used as upstream boundary condition. To provide the boundary conditions for the open sea boundary, a model cascade from the North Sea to the German Bay is setup and in each sequence, the results of the superordinate model are nested on the boundaries of the subordinate to provide the corresponding values for the open boundary conditions. The data for wind speed and direction are read from the ICON model results of the German Weather Service (DWD). The applied computational grid is structured curvilinear and covers an area of 2185 km^2 of the tidal influenced part of river Weser with the finest edge length of 20 m in upstream location and coarsest of 400 m at the open boundary (the North Sea side).

In the vertical domain the grid is composed of 10 vertical sigma-layers. The vertical dimension, e.g. depth dimension, is divided proportionally to the expected velocity and concentration gradients. Due to the presence of MP polymers with lower densities than water density ($\rho_{MP}<\rho_W$ or $(\rho_{MP}/\rho_w-1)<0$) on the water surface and presence of PE and PP as the dominant MP based on the literature, the uppermost layers close to the surface layer are important. Therefore, the surface region has a higher vertical grid resolution compared with the layers far from the surface. Analogously, due to the presence of settled MP on/in the riverbed as well as sediment and their resuspension, the layers in the proximity of the sediment bed have higher vertical grid resolution than the middle layers. The discretization of the central part of the water column is sufficient to allow for flow stratification due to baroclinic

effects. Fig. 3 exemplarily illustrates the vertical dimension of the 3D computational grid for a part of the River.

The bed roughness is estimated from the Van Rijn (1984) formulas for roughness prediction (Deltares, 2021a). Since morphology is also calculated (chapter 2.3.2), bed roughness is updated every five minutes. The time step for the hydro-morphodynamic model run is 6 s (0.1 min).

2.3.2. Morphodynamic module

The bed composition in the model setup is considered as a mixed sediment composed of four fractions: fine sediment (mud) with $d<63$ μm, fine sand with 63 μm$\leq d<200$ μm, medium sand with 200 μm$\leq d<630$ μm, and coarse sand with $d \geq 630$ μm. Fig. 4 shows the fine sediment fraction distribution in the bed of the Weser estuary. The data are from the Federal Waterway Administration (WSV) and AufMod project (Valerius et al., 2013, 2015).

In contrast to medium and coarse sandy sediment, the settling velocity of fine sediment (mud) is not a constant value and is defined based on the fine sediment concentration within the complex processes of flocculation, hindered settling and beginning consolidation of fine sediment. The implemented total settling rate formulation in this study covers the entire concentration range of fine sediments as was applied by Oberrecht (2021). At very low sediment concentrations ($C<C_f$), settling velocity is assumed as constant. Below the critical concentration for hindered settling (C_h), the settling behavior is described as a flocculation process, where the settling velocity increases with increasing sediment concentration (Van Rijn, 1993). If the concentration increases further ($C_h<C<C_{gel}$), sediment particles begin to hinder each other, because frictional forces become dominant. Here, the settling velocity decreases
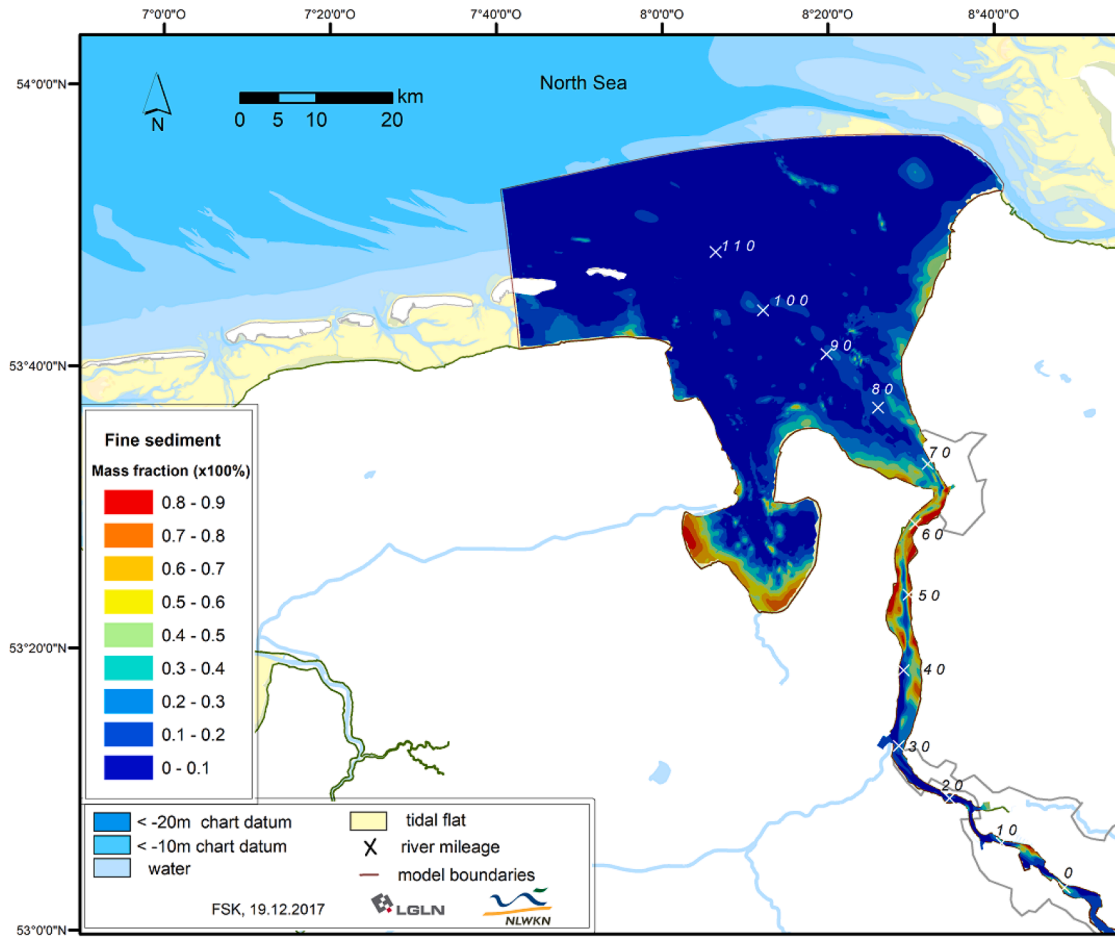
Fig. 4. Fine sediment fraction in the bed of the Weser estuary applied for initial condition of morphodynamic module. (For interpretation of the references to colours in this figure, the reader is referred to the web version of this article.)

with increasing concentration. Additionally, the hindered-settling behavior allows the formation of fluid mud.

For hindered settling, the formulation presented by Fredsoe and Deigaard (1992) was implemented. The hindered settling formulation is valid up to the gelling concentration (C_{gel}). When the suspension concentration exceeds the gel concentration, the fluid mud layer begins to consolidate. The rate of settling in the consolidation regime is calculated according to a simplified formulation proposed by Toorman (1992). The corresponding formulation for the settling velocity of the aforementioned processes for fine sediment could be described as:

$$w_s = \begin{cases} Const. & C \leq C_f \\ k_1 C^m & C_f < C \leq C_h \\ W_{s0}(1 - a_h C)^{b_h} & C_h \leq C \leq C_{gel} \\ W_{sg0}\left(\dfrac{C}{C_{gel}}\right)^{-\beta} & C > C_{gel} \end{cases} \qquad (1)$$

where w_s is the settling velocity of fine sediment (m/s), C is the concentration of fine sediment (kg/m^3), and k_1, m, a_h, b_h, β are constants and come from the research of Oberrecht (2021). These parameters are listed in Table S1 of the supplementary material. The graphic of this equation is illustrated in Fig. 5.

The critical shear stress for erosion and sedimentation of fine sediment is considered as 0.1 (N/m^2), this equal value for erosion and sedimentation is consistent with the critical shear stress for non-consolidated mud/fine sediment as is typical between 0.1–0.2 Pa

(Mengual et al., 2017).

2.3.3. MP-transport module

The 3D numerical MP-transport model FSK-MPTM is developed using the open-source CFD toolbox D-Water Quality (Deltares, 2021b). MP is considered in the model in terms of particle size, polymer density, and it's interactions with fine sediment and micro algae. The MP representation in the governing equations is formulated as a mass concentration. In order to consider the broad variability of MP particle properties, MP is considered in discrete classes of different MP particle sizes and polymer densities, which are then reflected in the settling velocity formulation. In combination with the fine sediment interaction and the biofouling effect, this leads to complex MP settling behavior, where the effective MP-settling velocity is a temporally as well as spatially varying property. The settling behavior distinguishes this study from most available literature, where usually constant settling velocities for MP independent of its interaction with SPM is considered.

The model considers MP input from basically two types of sources (i. e. point sources and diffuse sources). The point sources are MP inputs to the receiving Weser River at effluents of WWTPs located along the river.

2.3.3.1. Governing equations.
MP transport is mathematically formulated based on convection-diffusion equations, which are coupled with the ambient water parameters (flow velocity, temperature, salinity, and fine sediment concentration) and additional biological parameters (microalgae-concentration) which are required to approximate the MP interaction with fine sediment (Andersen et al., 2021) and biofouling (Kooi et al., 2017).
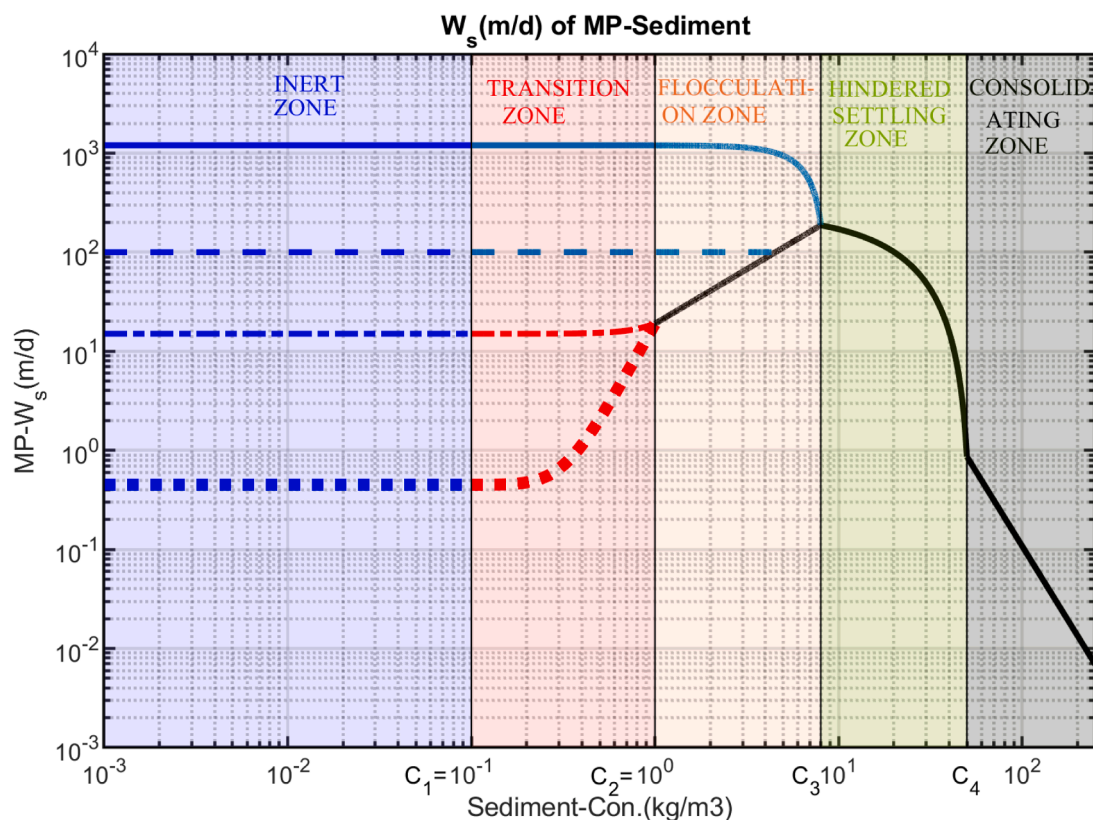
Fig. 5. MP-fine sediment settling velocity with respect to the fine sediment concentration: inert zone (blue), transition zone (light red), flocculation zone (pink), hindered settling zone (light green) and consolidation zone (gray). The black solid line is the settling velocity of fine sediment as summarized by Ross and Mehta (1989), the upper solid and dashed lines present exemplarily the settling velocity of MP with higher settling velocities than the flocculated sediment and the lower dashed-dotted and dotted lines exemplarily present the settling velocity of MP with smaller settling velocities than the flocculated sediment. (For interpretation of the references to colours in this figure, the reader is referred to the web version of this article.)

The transport mechanism of MP could be categorized in the following conceptual relationship:

$$\frac{dC_{MP}}{dt} = C_{\text{MP from sources}} + (\text{convection and diffusion of } C_{MP} \text{ in water})$$
$$+ \text{ resuspension from sediment} - \text{MP settling}(\pm \text{ MP fragmentation}$$
$$\pm \text{ bioturbation})$$

(2)

All of aforementioned parts of the transport balance equation apart from the MP fragmentation and bioturbation are included in this research.

MP-fine sediment interaction could be described by means of MP integration into fine sediment aggregates, which leads to the variation of MP settling velocity. This mechanism has been also observed and reported in literature by Andersen et al. (2021) and Li et al. (2019). It is accelerated by increasing the fine sediment concentration, where flocculation takes place. Therefore, the new development in D-Water Quality is performed by changing the MP settling velocity through a threshold sediment concentration. Fig. 5 illustrates the five zones for MP-fine sediment interactions, depending on the fine sediment concentration.

As can be seen in Fig. 5, the inert zone is defined as a low concentrated fine sediment, where the interaction between MP and sediment is ignored ($0 < C_s < C_1$). In this zone, it is supposed that fine sediment and MP follow their own settling velocity. The upper threshold concentration of this zone is set to 0.1 (kg/m^3) as was also observed by Andersen et al. (2021) for the increase of PVC particles settling velocity compared to settling in sea water without fine sediment.

In the transition zone ($C_1 \leq C_s < C_2$), the fine sediment starts to

influence the settling velocity of MP. However, this depends remarkably on the settling velocity of MP. If MP has a low settling velocity (like biofouled PP or PE), the capability of MP aggregation and contact with fine sediment is increased and therefore the MP-settling velocity is more influenced by the fine sediment settling velocity. In contrast, MP with significantly higher densities and therefore higher settling velocities than fine sediment could pass through the fine sediment and therefore the contribution of fine sediment to the MP-settling velocity is decreased. The transition zone can also be defined by user and as it was determined after calibration for the Weser River as 0.1 (kg/m^3) $< C_s \leq 1$ (kg/m^3). The lower threshold concentration ($C_s = 0.1$ (kg/m^3)) was also experimentally observed by Andersen et al. (2021) as the initial fine sediment concentration for MP-fine sediment aggregation.

The third zone is defined as flocculation zone. In this zone ($C_2 \leq C_s < C_3$), it is supposed that MP with lower settling velocity than fine sediment is captured within the fine sediment flocculation, and hence settles with the fine sediment. Contrary to fine and light MP, particles with higher densities as well as coarser MP pass through the fine sediment and are not aggregated. This zone can also be defined using a threshold concentration like C_3, which is proposed for the Weser River as 8 (kg/m^3), i.e. the MP with lower settling velocity than fine sediment behave like fine sediment in the fine sediment concentration range of 1 (kg/m^3) $< C_s \leq 8$ (kg/m^3). It should be noted that the upper boundary value $C_s = 8$ (kg/m^3) was also applied by Oberrecht (2021) in the morphodynamic model, which was also used in this study for modeling the fine sediment concentration.

In hindered settling zone, the settling velocity of fine sediment as well as captured MP is retarded due to the high concentration of fine sediment, where by increasing the sediment concentration, the settling velocity is reduced. Due to the high sediment concentration, it is

supposed that in this zone all of the available MP are integrated to the fine sediment and consequently settle with the velocity of fine sediment. This zone of concentration could be defined by user through threshold concentration C_4 (kg/m^3), which was taken for the Weser River as 50 (kg/m^3) (Oberrecht, 2021).

Finally, the settled sediment in highly concentrated sediment layers in bed start to consolidate and MP is totally enclosed in the sediment bed. This layer is defined at sediment concentrations greater than 50 (kg/m^3), where the pore water volume is reduced and sediment shows a higher resistance to the current/wave induced bed shear stresses.

In the inert range, the settling velocity of MP (W_{MP}) is computed using the formulation applied by Kooi et al. (2017), which was proposed by Dietrich (1982) and is given as:

$$W_{MP}(z, T, S, t) = \left(\left(\frac{\rho_{MP}}{\rho_w(z, T, S, t)} - 1 \right) g w_{MP}^* \vartheta_w(z, T, S, t) \right)^{1/3} \tag{3}$$

where z (m) is the depth direction with the origin on mean water surface and upward positive direction, t (s) the time of simulation, $\rho_w(z, T, S, C_s, t)$ is the water density (kg/m^3) as a function of water depth, temperature (T (°C)), salinity (S (PSU)), sediment concentration (C_s) and ρ_{MP} is the MP-density (kg/m^3), g gravitational acceleration (m/s^2), w_{MP}^* is the dimensionless settling velocity of MP and $\vartheta_w(z, T, S, C_s, t)$ is the kinematic viscosity of water (m^2/s).

The water density is computed by including the salinity, temperature and fine sediment concentration at the corresponding water depth. Therefore, it is not a constant value in the model, but it is computed as a function of salinity and varies over space and time. Kooi et al. (2017) applied the semi-empirical formulas to find the salinity and temperature in different water depths, while in this research these values are numerically for the Weser River modelled, calibrated and then are applied in the equations. Applying the effect of sediment concentration on the water density, $\rho_w(z, T, S, t)$ is computed by means of application the model results for temperature and salinity in the proposed equation by Sharqawey et al. (2010):

$$\rho_w(z, T, S, t) = \rho_0 + \left(a_1 T + a_2 T^2 + a_3 T^3 + a_4 T^4 \right) + \left(b_0 S + b_1 S\,T + b_2 S\,T^2 + b_3 S\,T^3 + b_4 S^2 T^2 \right) \tag{4}$$

where ρ_0 is the pure water density 999.9 (kg/m^3) and a_n, b_n ($n = 1, ..., 4$) are given in Table S1 of the supplementary material.

Kinematic water viscosity (ϑ_w) is also computed for each time-step by means of the computed model results for temperature and salinity in the corresponding water depth using the equation proposed by Sharqawey et al. (2010):

$$\vartheta_w(z, T, S, t) = \frac{1}{\rho_w(z, T, S, C_s, t)} \left(m_1 + \left(m_2 (T + m_3)^2 - m_4 \right)^{-1} \right) \left(1 + A + BS^2 \right) \tag{5}$$

where m_n ($n = 1, ..., 4$) coefficients as well as A and B functions are provided in Table S1 of the supplementary material.

w_{MP}^* is given by means of Dietrich (1982) formula, applied by Kooi et al. (2017) as:

$$\log\left(w_{MP}^*\right) = \begin{cases} -3.7595 + 2.0\log D^* \ for \ D^* < 0.05 \\ -3.76715 + 1.92944\log D^* - 0.09815(\log D^*)^{2.0} \\ -0.00575(\log D^*)^{3.0} + 0.00056(\log D^*)^{4.0} \ for \ 5*10^9 \le D^* \le 0.05 \end{cases} \tag{6}$$

where D^* is the dimensionless particle diameter and is calculated for MP as:

$$D^* = \frac{(\rho_{MP,tot} - \rho_w) g D_n^3}{\rho_w \vartheta_w^2} \tag{7}$$

where D_n is the nominal diameter of MP particle and defined as the diameter of a sphere with equivalent volume of MP particle. $\rho_{MP,tot}$ is the MP particle density including the effect of biofouling after Kooi et al. (2017). The details of the specific adaptation of the Kooi et al. (2017) approach for this model will be published in a separate paper. For a basic explanation see supplementary data.

D_n is then calculated as:

$$D_n = (1.5\ d_1 d_2 d_3)^{1/3} \tag{8}$$

where $d_1 (m)$ and $d_2 (m)$ are the major(long) and minor(short) diameters of an elliptic cylinder with height of $d_3 (m)$. In contrast to the most available literature, which assume in their calculations the shape-form of MP particles as a sphere, in this research because of high occurrence of fragment-like MP (Roscher et al., 2021), an elliptical cylinder is assumed. d_1 and d_2 are measured by µFTIR and d_3 depends on the Corey Shape Factor (CSF) of MP particles:

$$CSF = \frac{d_3}{\sqrt{d_1 d_2}} \tag{9}$$

where a sphere has CSF=1 and it changes between 0 and1 for other particle shapes. With this assumption, the volume of a MP particle is approximated by:

$$V = (CSF)0.25\ \pi d_1 d_2 \sqrt{d_1 d_2} \tag{10}$$

2.3.3.2. MP-Sedimentation and resuspension. The riverbed is an important reservoir for MP in freshwater as well as in estuaries. Sedimentation of MP could happen for the light MP by means of aggregation/capturing into fine sediment as well as biofouling and for heavy MP (heavier than water) through their own weight within low energetic flows. Here, sedimentation is captured by means of the critical shear stress for sedimentation ($\tau_{csed}\left(\frac{N}{m^2}\right)$), which is compared with the calculated shear stress of the flow field in the adjacent computational cell. Then, if the available MP mass in the corresponding computational cell has a positive settling velocity (settling velocity towards the bed), it starts to settle with a settling velocity calculated using Eq. (3).

Critical shear stress for sedimentation is an empirical tuning parameter that depends on the MP-polymer density, MP particle size, and the interaction between MP and SPM in the water column. In this investigation it is assumed to be close to that of the surrounding fine sediment. $\tau_{sed} = 0.1\left(\frac{N}{m^2}\right)$ is in agreement with literature values and shows a good consistency between measured MP mass-concentrations and model results. However, it could be modified based on the fine sediment concentration or defined as spatially varying in the studied catchment.

The sedimentation flux for settling MP ($F_{sed}\left(\frac{kg}{m^2 s}\right)$), is computed as:

$$F_{sed} = W_{MP} C_{MP} \alpha_{MP} \tag{11}$$

where W_{MP} is calculated by means of Eq. (3), $C_{MP}\left(\frac{kg}{m^3}\right)$ is the MP mass concentration computed by means of the convection-diffusion equation and α_{MP} is the MP-sedimentation probability function based on an excess shear stress formulation, according to the Partheniades (1965); Krone (1962) formulation (Delft3D-FLOW manual (Deltares, 2021a)) as:

$$\alpha_{MP,sed} = \begin{cases} \left(1 - \frac{\tau}{\tau_{csed}}\right) & if\ \tau < \tau_{csed} \\ 0 & if\ \tau \ge \tau_{csed} \end{cases} \tag{12}$$

Settled MP in sediment could also be resuspended under higher current velocities. Therefore, the bed shear stress determines the resuspension and its corresponding flux into the water column. Critical bed shear stress for MP depends on the MP physical characteristics (i.e. density and size) as well as the surrounded sediment (Enders et al., 2019). The contribution of these parameters is usually determined by means of physical experiments. Waldschläger and Schüttrumpf (2019)

performed an experimental research to investigate the critical shear stress for resuspension of already available MP particles ($\rho_{MP} > \rho_w$) on sediment composed of sands with different grain size distributions (medium and coarse sand as well as fine gravel). They proposed an empirical equation, which could be applied with a good accuracy for MP as:

$$\theta_{cr,MP,s} = \varphi\theta_{cr,s}\left(d_{MP}/d_{50,s}\right)^{\gamma} \tag{13}$$

where $\theta_{cr,MP,s}$ is the critical Shields parameter for MP in sand and is defined as:

$$\theta_{cr,MP,s} = \frac{\tau_{cr,MP,s}}{\left(\frac{\rho_{MP}}{\rho_w} - 1\right)g\, d_{MP}} \tag{14}$$

$$\tau_{cr,MP,s} = \theta_{cr,MP,s}\left(\frac{\rho_{MP}}{\rho_w} - 1\right)g\, d_{MP} \tag{15}$$

and therefore the critical bed shear stress for resuspension of MP $\left(\tau_{cr,MP,s}\left(\frac{N}{m^2}\right)\right)$ in sand could be given as: where $\theta_{cr,s}$ in Eq. (13) is the critical Shields parameter of sand, $d_{MP}(m)$ for MP particle size and $d_{50,s}(m)$ is the median diameter of sand, where 50% of sand is smaller than this size. φ and γ are coefficients, which were proposed by Waldschläger and Schüttrumpf (2019) as 0.5588 and −0.503, respectively.

However, estuarine sediment often naturally occurs as a mixture from fine sediment and sand. Therefore, the proposed equation by Waldschläger and Schüttrumpf (2019) cannot be applied for fine silty sediment. In this research, the critical bed shear stress for resuspension of MP is defined spatially varying based on the modelled bed sediment composition (a mixture composed of one cohesive sand fraction and three sand fractions i.e. fine, medium and coarse sand).

Mixed sediment (cohesive with non-cohesive) have higher critical bed shear stress against the erosion. One of the main reason for this could be the presence of fine/cohesive sediments (like silt and clay), which fill the pore spaces between the non-cohesive sediment (e.g. sands) and therefore improve the general structure of mixed sediment against erosion. Therefore, coarse fractions keep longer against the near bed current which in terms reduces the total erosion rate of sediment in a mixture compared with each fraction as a single fraction. To take this natural characteristic of sediment into account, and consequently apply for the settled MP between mixed sediment, the critical bed shear stress for a mixture of sand and mud based on the bed composition of the Weser River is setup in the model as the critical bed shear stress. The proposed equation by Wu et al. (2018) for critical bed shear stress of mixed sediment is modified for MP as:

$$\tau_{cr,MP,m} = \tau_{cr,MP,s} + \left(\tau_{cr,MP,pm} - \tau_{cr,MP,s}\right)\mathbf{exp}\left[-f_1\left(\frac{p_s}{p_m}\right)^{f_2}\right] \tag{16}$$

where $\tau_{cr,MP,m}$ $\left(\frac{N}{m^2}\right)$ is the critical resuspension shear stress for MP located among mixed sediment (i.e. mud and sand), $\tau_{cr,MP,pm}\left(\frac{N}{m^2}\right)$ the critical resuspension shear stress for MP located in pure mud, p_s the percentage of the sand in the MP-surrounded mixed sediment, p_m the percentage of fine sediment/mud in the mixture and f_1, f_2 are calibration coefficients.

Due to the lack of an equation for critical resuspension shear stress for MP in pure mud like the already proposed equation for (pure) sand by Waldschläger and Schütterumpf (2019), the empirical equation proposed by Wu et al. (2018) for pure mud is modified as:

$$\tau_{cr,MP,pm} = k_1\left(\varphi_m^{-1} - 1\right)^{k_2}\left(\frac{\rho_{MP}}{\rho_{pm}}\right)^{k_3}\left(\frac{D_{MP}}{D_{pm}}\right)^{k_4} \tag{17}$$

where k_n are the calibration coefficients and given in supplementary material and φ_m is the mud porosity, which is given as:

$$\varphi_m = 1 - \left(\rho_{dmb}/\rho_s\right) \tag{18}$$

where $\rho_{dmb}\left(\frac{kg}{m^3}\right)$ is the bulk dry density of mud and $\rho_s\left(\frac{kg}{m^3}\right)$ the sand density.

The last two terms in Eq. (17) are proposed in this research to extend the approach of Wu et al. (2018) for MP. With respect to Eq. (17), it is assumed that the MP with higher density than pure mud requires higher shear stresses for resuspension. Moreover, in case of MP with the same density of mud, the coarser MP are resuspended under higher bed shear stresses. Calibration parameters in Eq. (17) are found by means of the comparison of the model results with MP concentrations measured during the PLAWES campaign (Roscher et al., 2021, this paper).

Finally, the resuspension upward directed flux is defined in the same way to the sedimentation flux as:

$$F_{res} = W_{MP}C_{MP,b}\alpha_{MP} \tag{19}$$

where:

$$\alpha_{MP} = \begin{cases} \left(\frac{\tau}{\tau_{cr,MP,m}} - 1\right) if\ \tau > \tau_{\tau_{cr,MP,m}} \\ 0\ if\ \tau \leq \tau_{\tau_{cr,MP,m}} \end{cases} \tag{20}$$

Then, the available fine sediment concentration in the water column is read from the communication data of hydro-/morphodynamic results and the MP-settling velocity is again calculated based on the available fine sediment concentration in each computational cell. Therefore, based on this approach, the settling of MP in the parts of the river with high concentration of fine sediment is increased.

2.3.3.3. MP boundary conditions. The modeling approach requires boundary conditions, which are usually derived from measurements. Within the MP modeling the lack of sufficient measured data is still a major problem and can up to now only be compensated by assumptions, which introduce additional uncertainty into the model solution (see also conclusions). On the other hand, this uncertainty also legitimates adaptions of boundary conditions during the model calibration process.

Since the model internally considers MP mass concentrations, further assumptions and calculus are involved (Eq. (9). and Eq. (10)): When measured MP input is given in terms of particle counts (Roscher et al., 2021), these were transformed into MP mass concentrations using the CSF of MP fragment particles (Kooi and Koelmans, 2019). The CSF in Eq. (10) is assumed as 0.6 and MP polymer densities are considered as provided in the supplementary data of Mintenig et al. (2020).

For the calibration of the MP transport model the MP input by means of the WWTP (point sources) were varied based on the following procedure. As a first guess, the measurements from Mintenig et al. (2017) for seven WWTPs (Brake, Varel, Berne, Neuharlingersiel, Schillig, Sandstedt and Burhave) along the model domain were transferred to the other 19 WWTPs. This was done by scaling the observed MP particle loads based on the number of inhabitants connected to each WWTP in Mintenig et al. (2017) measurements.

This first approach has some major flaws though. It is not known, how representative these seven WWTPs are for the other 19, moreover, the WWTPs differ with respect to technical details of the treatment. Additionally the Mintenig et al. (2017) data are from 2014 and the PLAWES measurements for tidal part of the Weser (Roscher et al., 2021) are from 2018. This time difference of measurements causes further uncertainty. Furthermore, the necessary but inevitably simplified conversion from MP particle counts into MP mass concentrations has a strong inherent uncertainty.

Also, on the MP transport model side, due to the lack of measurements not all possible MP sources are considered so far (e.g. tire wear, MP input from inland dewatering and surface runoff), so within the calibration process the WWTP point sources were varied with respect to the initial guess in order to fit the modeled MP results towards the MP mass concentrations observed within the April 2018 PLAWES campaign
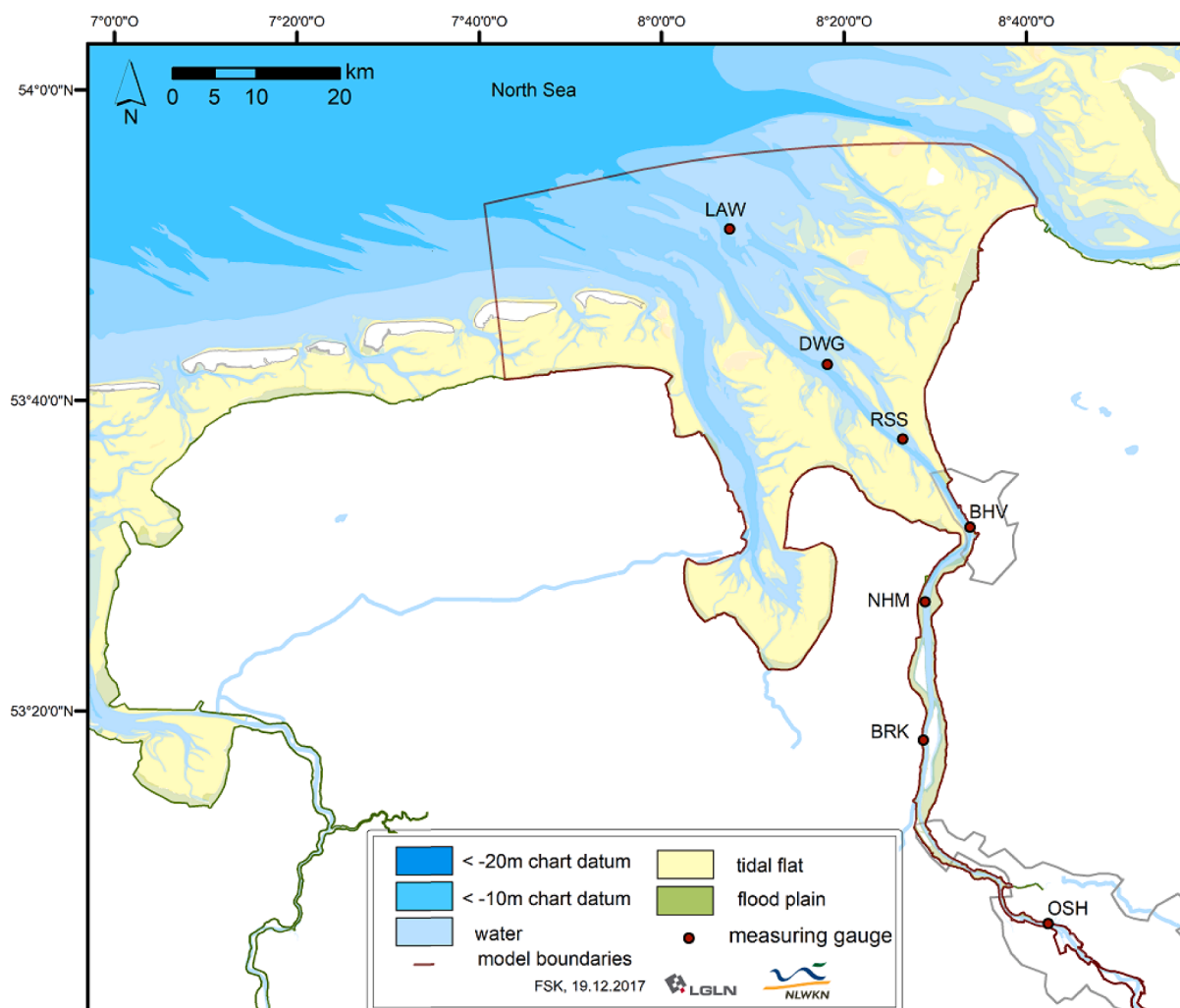
Fig. 6. Location of measuring gauges (small red filled circles) for comparison with the model results. (For interpretation of the references to colours in this figure, the reader is referred to the web version of this article.)

(Table 4, Fig. 12). It should be also noted that the PLAWES measurements on the Weser River represent the overall MP load and it is not possible to assign them to WWTPs or other specific MP sources only.

The diffusive sources in this study consider atmospheric deposition flux for the cities along the Weser River. In this research measurements were performed for six stations in the Weser catchment (Kernchen et al., 2022), where two of them were positioned in the tidal part of the Weser River close to the two major cities Bremen and Bremerhaven. The determined MP concentration values were considered representative as MP diffusive contamination sources. MP fluxes from other cities were estimated by means of extrapolating w.r.t the corresponding population density compared to aforementioned cities. The resulting diffusive MP flux into the water body is approximated based on a first order transport length approach (Wang and Lai, 2014) using statistical measured data for wind speed and direction (Table 1).

2.4. MP mass determination of selected water samples

In a selected sample sub set of surface waters (<500 μm fraction) from the PLAWES campaign (six stations; 16, 34, 41, 45, 50 and 51, Fig. 1) the mass concentration of eight polymer type clusters was determined via pyrolysis-gas chromatography-mass spectrometry (Py-GC/MS). All samples represented already processed aliquots from the particle related study (Roscher et al., 2021). These aliquots were transferred onto glass fiber filters, spiked with an internal standard and

pyrolyzed applying thermochemolysis at 590 °C. Measurements were performed with pyrolysis-gas chromatography-mass spectrometry (Py-GC/MS) based on previously published methods (Fischer-andScholz-Böttcher, 2017, 2019; Dibke et al., 2021). Mass-quantification of polymers was executed by backbone-related polymer specific clusters (Primpke et al., 2020; Dibke et al., 2021; Primpke et al., 2022). Polymer clusters were indicated by the prefix "C" and included among others polyethylene (C-PE), polypropylene (C-PP), polyethylene terephthalate (C-PET), polystyrene (C-PS), polyvinylchloride (C-PVC), polycarbonate (C-PC), polymethlymethacrylate (C-PMMA) and MDI (methylene diphenyl diisocyanate derived)-polyurethane (C-MDI-PUR). Corresponding concentrations data are listed in Table 4.

3. Results and discussion

In the estuarine range the hydrodynamics interact with salinity and suspended sediment in several complex ways due to their influence on the fluid density (e.g. existence of baroclinic effects and resulting ETZ, Becker et al., 2013). MP in this surrounding is a completely passive substance with little to no influence on the flow field. It is therefore of major importance, to first achieve a sound calibration of the coupled hydro-morphodynamic model part, which drives the MP transport. The model results are calibrated by means of available measurements for water level (m), salinity (PSU), sediment concentration (kg/m^3),
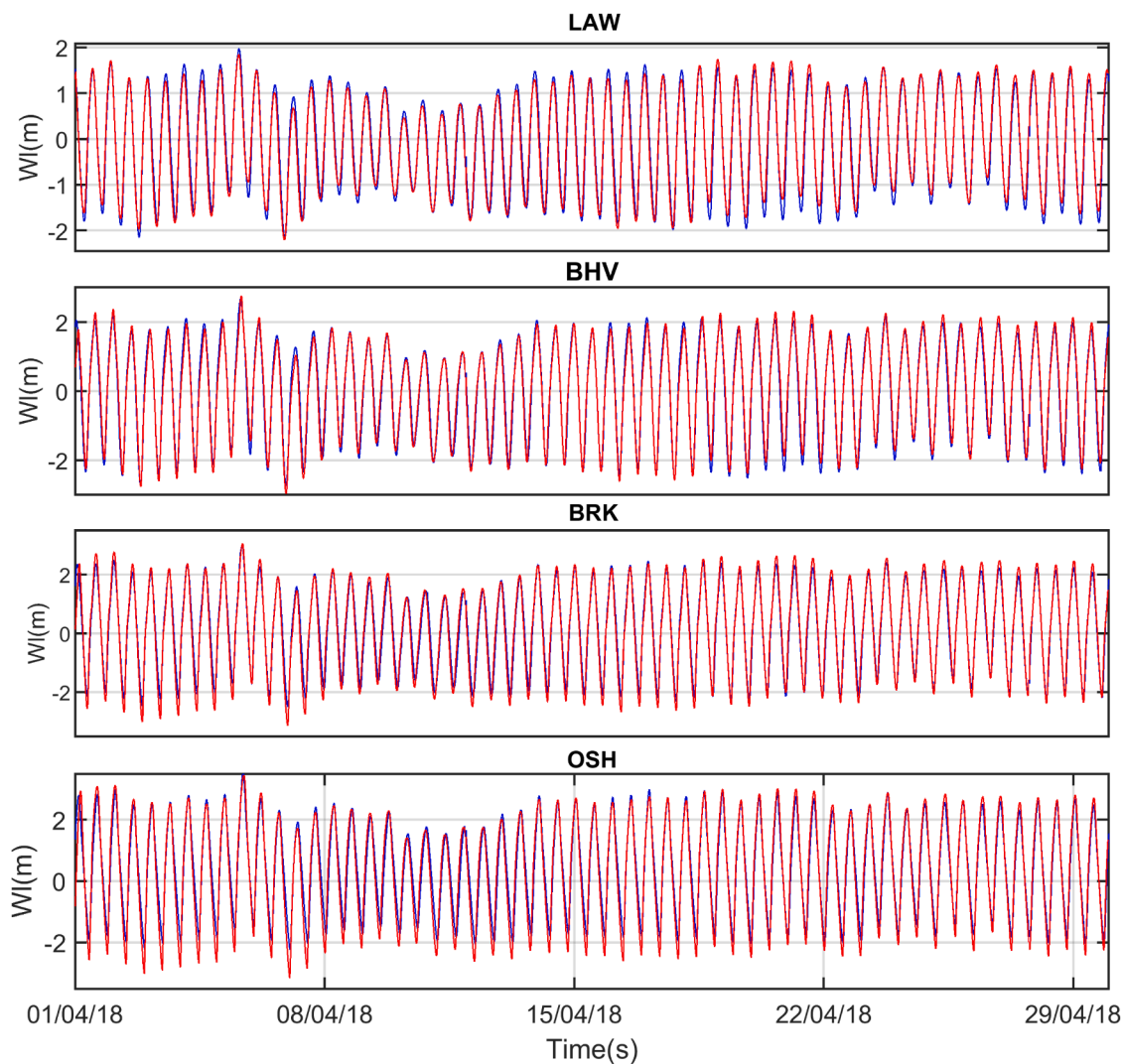
Fig. 7. Comparison between model results (red) for water level (m) and measurements (blue) for pegels in different locations of the study domain; LAW close to the open boundary, BHV in the mouth of estuary, BRK in middel of estuary and upstream and OSH close to the upstream discharge (measurements from WSV). (For interpretation of the references to colours in this figure, the reader is referred to the web version of this article.)

temperature (°C), and MP-concentration (g/m³). The sources of the calibration data are given in Table 1.

3.1. Hydrodynamic model for water level

Because of the important role of the flow field for the transport and resuspension of SPM (e.g. sediment and MP), calibration and validation of the hydrodynamic model is an important prerequisite for the calibration of MP-transport model runs. Forcing boundary values, application of wind stresses on the water surface, bed parameters for computing the flow energy dissipation (e.g., bed roughness), turbulence approach and computational grid resolution are inseparable parts in calibration of a hydrodynamic model.

The hydrodynamic model is driven by inland discharges (Weser, Lesum, Hunte, Ochtum, Geeste) and the open sea boundary tidal water level elevations (Table 1).

To calibrate the hydrodynamic model, the computed water levels are compared with the recorded time series at gage stations along the river. By tuning the bottom friction values using the auto-predictor property of trachytope approach and selecting the Van Rijn (1984) approach (Deltares, 2021a), it is tried to find the best agreement between model results and measurements. In this approach, the bed-forms are actualized after

each five time steps of flow calculation, and the bed-roughness is calculated based on the formula of Van Rijn (1984). The interested reader is recommended to read the trachytopes classes in the Delft3D-FLOW manual (Deltares, 2021a).

Fig. 7 shows the comparison between model results with the measurements at different stations along the Weser estuary as are shown in Fig. 6 and their locations (with the depth of installation) are listed in Table S3. The 3D-property of the model allows to compare model results and measurements at the same elevations as the measuring gauges (Table S3).

As can be seen in Fig. 7, the model is capable of reproducing the measurements very well in terms of the water elevation as well as phase agreement. The statistical parameter of the Pearson correlation factor (r) between model results and measurements were calculated and is found in Table S4. It shows a strong relationship between model and measurements results by $r = 97\text{–}99\%$ (Akoglu, 2018). Moreover, the Brier Skill Score (BSS) (Van Rijn et al., 2003), which is defined as:

$$BSS = 1 - <|Model - Measurements|^2> \Big/ <Measurements^2> \tag{21}$$

where $<>$ depicts the mean of assigned value, classifies the model performance based on BSS in different classes, i.e., BSS=1–0.8 excellent,
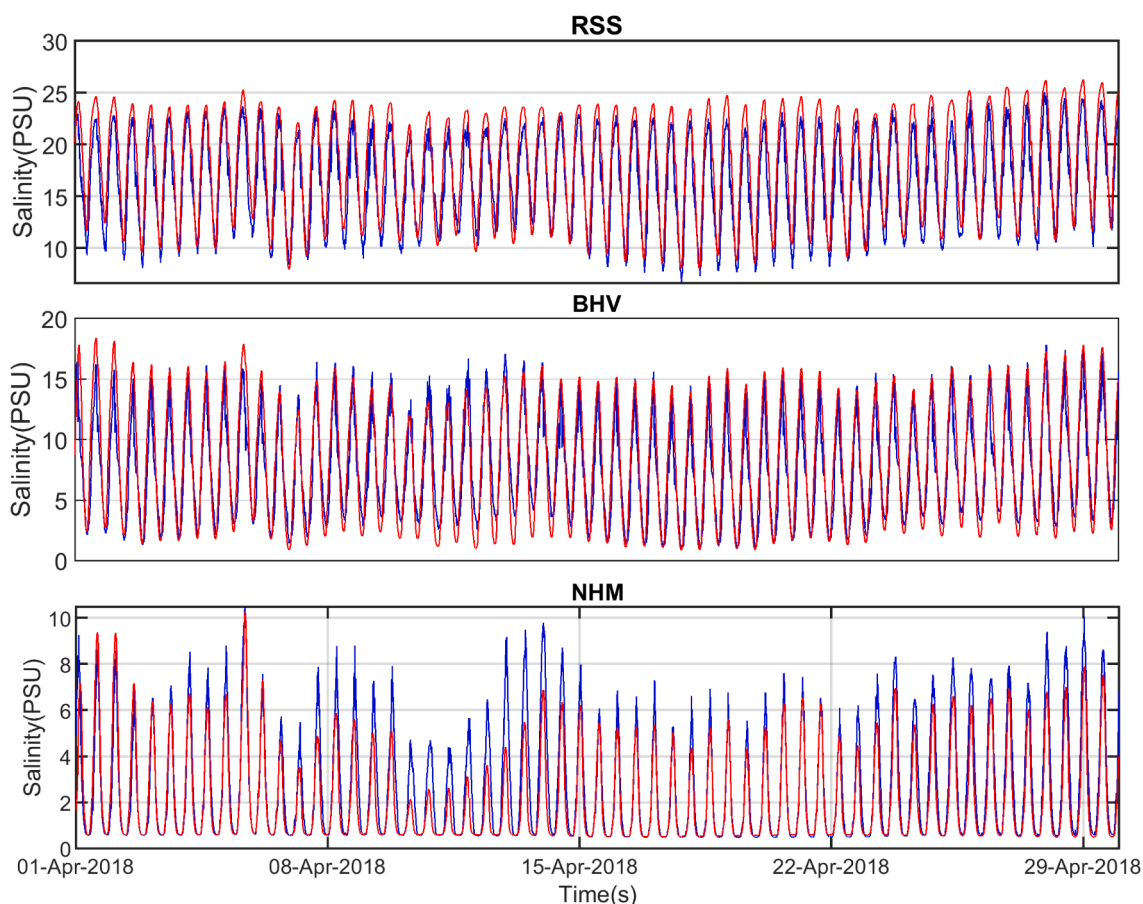
Fig. 8. Comparison between model results (red) for salinity (PSU) and measurements (blue) in different locations within the turbidity zone; BHV is in the mouth of estuary, and (RSS) and NHM are located downstream and upstream of BHV pegel, respectively (measurements from WSA). (For interpretation of the references to colours in this figure, the reader is referred to the web version of this article.)

0.8–0.6 good, 0.6–0.3 fair, 0.3–0 poor, and <0 bad. It is shown in Table S4 that the model performance based on the corresponding BSS for the water level is excellent.

Systematic velocity measurements for direct comparison with the model results are not available. The excellent statistical agreement between calculated and measured water levels at all available gauges across the model domain (Table S4) proves the good reproduction of the tidal volume and implicitly ensures realistic flow velocities during the tidal cycle.

3.2. Hydrodynamic model for salinity

Salinity on a local scale influences the turbulence production which on a larger scale leads to baroclinic estuarine circulation due to its effect on the density. The salinity distribution along the estuary varies horizontally as well as in vertical direction and time. Therefore a thorough reproduction of the measured salinity time series by the model ensures a realistic baroclinic circulation intensity, which is also a relevant prerequisite for realistic suspended sediment and MP transport.

The salinity transport model is driven by boundary conditions at all open boundaries (Weser, Lesum, Hunte, Ochtum, Geeste and the open sea boundary, see Table 1).

Fig. 8 shows the comparison between the model results and measurements for three stations around the ETZ. As can be seen, the model results agree well with the measurements regarding their phase, but for the absolute values show a slightly higher longitudinal gradient as observed. The statistical parameters for correlation coefficient is between 93–96% and BSS varies between 0.76–0.92, which classify the

model performance between good to excellent (Table S5).

However, the model is able to very well reproduce the salinity for stations RSS and BHV, where the baroclinic circulation is basically driven.

3.3. Hydrodynamic model for temperature

The importance of the modelled temperature lies in the ecological submodule, which computes the microalgae concentration. Since the algae growth is strongly dependent on temperature, a realistic reproduction is important for the biofouling activity on MP (see supplementary data).

The temperature model is driven by boundary conditions at all open boundaries (Weser, Lesum, Hunte, Ochtum, Geeste and the open sea boundary, see Table 1).

As can be seen in Fig. 9, the model results are in good agreement with the measurements in terms of phase and absolute values. The statistical parameters for correlation coefficient is between 98−99% and BSS varies between 0.68–0.98, which classify the model performance between good to excellent (Table S6).

3.4. Morphodynamic model fine sediment concentrations

The model results for suspended sediment concentration are compared with measurements (Fig. 10) for three ETZ stations in the Outer Weser. The model results are reasonable in comparison with measurements, particularly for BHV gage station. However, the measured peak values are underestimated most of the time and also the
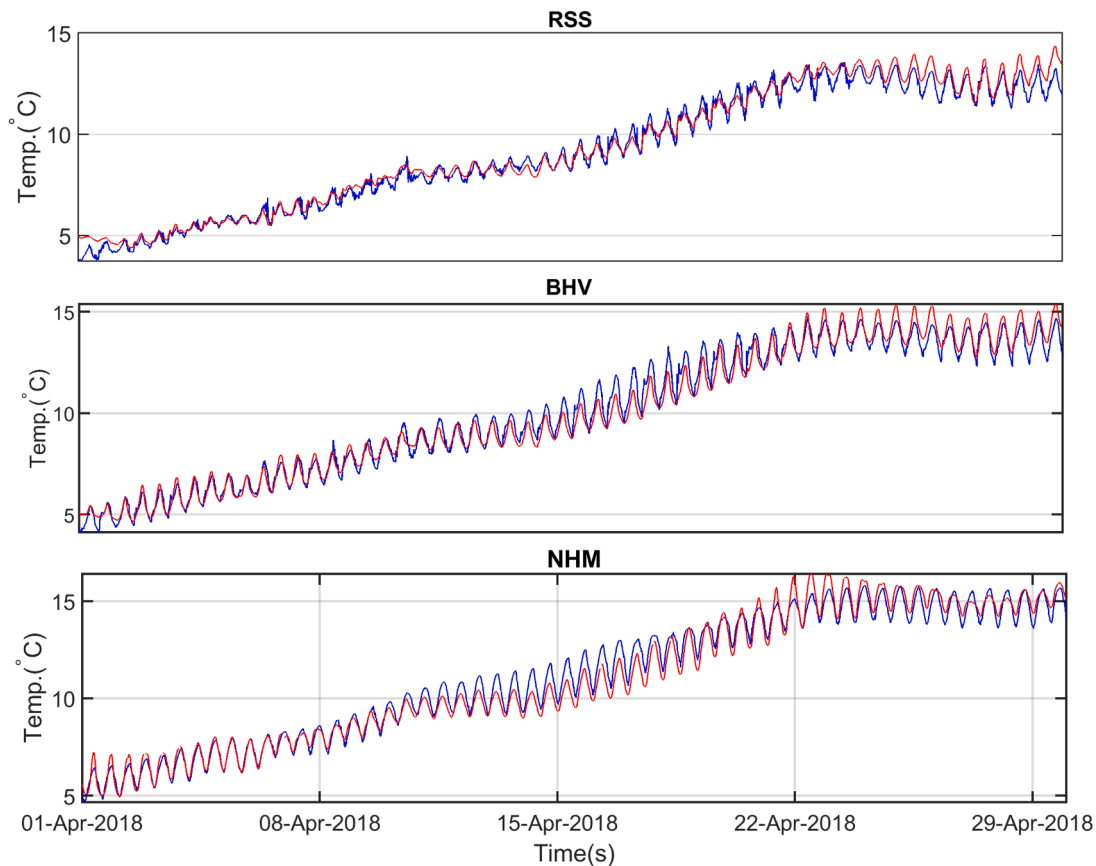
Fig. 9. Comparison between model results (red) for temperature (°C) and measurements (blue) in different locations within the turbidity zone; BHV is in the mouth of estuary, and RSS and NHM are located downstream and upstream of the BHV pegel, respectively (measurements from DWD). (For interpretation of the references to colours in this figure, the reader is referred to the web version of this article.)

characteristic spring-neap cycle (14-day periodicity) is not covered very well.

Since SPM concentration are very sensitive to local scale variability in sediment availability and turbulence structure, it is a known difficulty in estuarine turbidity modeling to get sufficient agreement between the point measurement and the corresponding computational cell, which can inevitably not consider those sub-grid variabilities in turbulence and SPM values.

Another aspect here is the vertical location of the SPM sensors, which are all located well above the baroclinic stratification range within the water column. As a result the comparison of measured and calculated SPM values becomes strongly dependent of the turbulence damping approach, which inherits strongly empirical characteristics. However, the relevant SPM concentrations for MP interaction occur in the lower water column, where the calculated SPM values are well above the threshold for MP-sediment-interaction.

The morphodynamic model performance could be further improved by a longer model spin-up time (Schoellhamer et al., 2008) and tweaking of the turbulence damping formulation, but the achieved result is already sufficient for the use intended here: The estuarine turbidity maximum is calculated at the right location and the SPM-concentrations are high enough to trigger the MP interaction. This good qualitative agreement between model and reality also ensures realistic spatial distributions of MP. The statistical parameters for correlation coefficient and BSS classify the model performance as good except for that of BHV (Table S7).

3.5. MP-transport model

The MP-transport model is run with boundary conditions at open boundaries (stations 19 and 20 for the seaside boundary and station 53 for the upstream discharge) derived from Roscher et al. (2021), modified sources from WWTP after Mintenig et al. (2017) and diffusive atmospherical MP input after Kernchen et al. (2022), see also chapter 2.3.3.3 and Table 1.

Initial conditions were generated by means of a one month spin-up run which was initiated with a spatial interpolation of the dataset from Roscher et al. (2021) for the water body and Halbach & Scholz-Boettcher (see Table 1) for the sediment bed.

A coarse calibration to meet at least the order of magnitude of observed MP data was possible against a subset of the Roscher et al. (2021) data set.

Table 2 shows the base polymer types and corresponding properties considered in the model configuration. Two size classes were distinguished for each polymer type: <500 μm (small MP) and >500 μm (large MP). The size classification here reflects the analytical results that were grouped into small and large MP after Roscher et al. (2021).

The sampling stations for model validation are highlighted in Fig. 11. St. 34, St. 41, and St. 45 are located inside the ETZ. Due to higher fine sediment concentrations in the ETZ, these help to evaluate the performance of the described approach for MP-fine sediment interaction. The model here shows good qualitative agreement w.r.t. significantly increased MP occurrence within the ETZ (as is also reported by Roscher et al. (2021)).

Fig. 12 shows the model validation with the Py-GC/MS results, which are methodically completely independent of the calibration and boundary condition data. The model reproduces the order of magnitude of the direct measurements with good accuracy. This applies even more, given the little available calibration data and resulting coarse calibration. The model results were taken from the same time frames and also
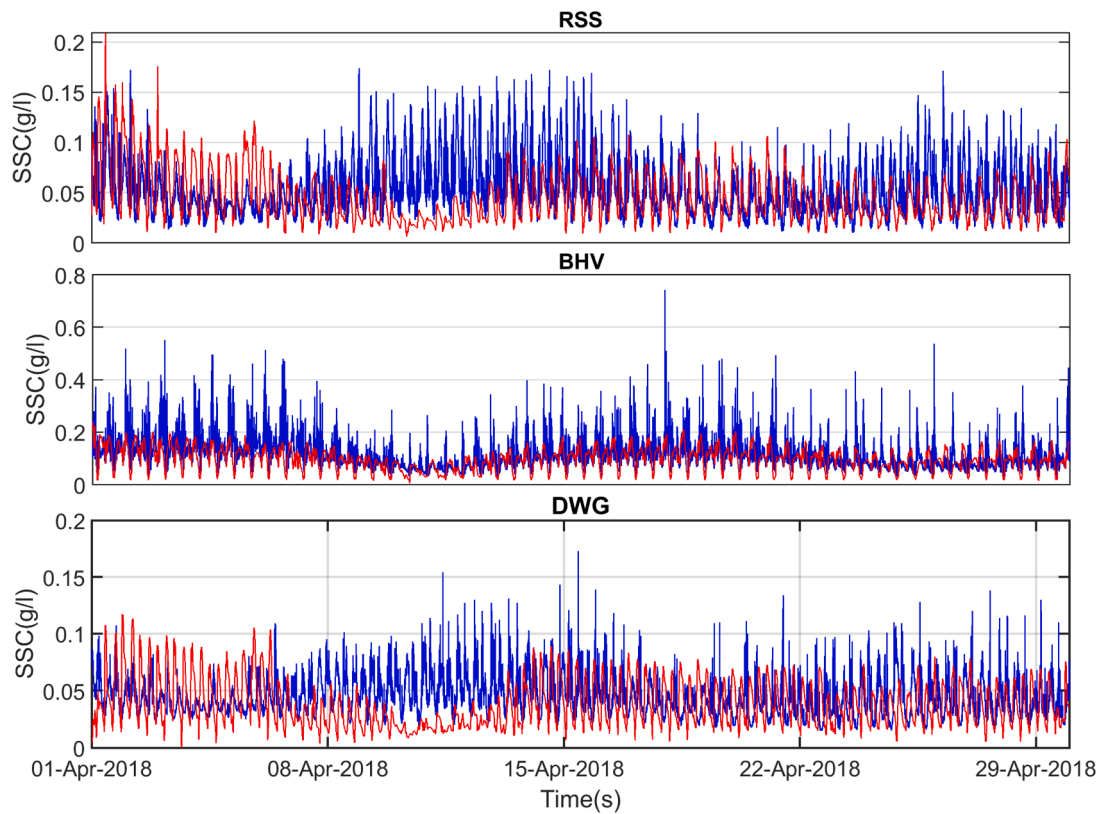
Fig. 10. Comparison between model results (red) for fine sediment concentration (g/l) and measurements (blue) in different locations within the estuary turbidity zone (ETZ); BHV is in the mouth of estuary, and RSS and DWG are located downstream of the BHV pegel (measurements from WSA). (For interpretation of the references to colours in this figure, the reader is referred to the web version of this article.)

Table 2
Properties of the modelled MP for calibration.

Polymer type	Abbreviation	Density (g/cm³)	Inert settling velocity using Dietrich (1982) formula (mm/s)
Polyethylene	PE	0.910	buoyant ($\rho_{MP} < \rho_w$)
Polypropylene	PP	0.920	buoyant ($\rho_{MP} < \rho_w$)
Polystyrene	PS	1.04	0.0027
Polyvinyl chloride	PVC	1.38	0.0238
Polyurethane	PUR	1.20	0.0117
Polyethylene terephthalate	PET	1.33	0.0204
Polycarbonate	PC	1.21	0.0949
Poly(methyl methacrylate)	PMMA	1.18	0.0104

from the water depths as the water samples were taken.

The good reproduction of MP concentrations compared with the measurements in Fig. 12 (the corresponding values are listed in Table 3) is a result of the described deterministic model approach. The statistical analysis of the model results in Table 3 reveals, that the model results are generally over-estimated (all mean (Δ)>0, where Δ=Model results-PLAWES campaign). Moreover, the model shows an excellent performance for (C-)PS (BSS=0.96), (C-)PC (BSS=0.81), and (C-)PMMA (BSS=0.89), good for (C-)PET (BSS=0.67), fair for (C-)PE (BSS=0.42), (C-)PVC (BSS=0.32), and bad for (C-)PP (BSS=−0.33), (C-)MDI-PUR (BSS=−2.25). The overall BSS of the model results is 0.69, which classifies the model performance as good. A possible explanation for the (C-)MDI-PUR result is given in the discussion further below.

The spatial MP distribution and transport are strongly coupled with the estuarine hydro- and sediment dynamics. As a result, the model achieves a good overall distribution even with little MP boundary data availability as is the case with this investigation.

Despite the good overall agreement significant deviations for some polymer types at some locations can be observed. MDI-PUR for example is measured only at stations 45 (BRK) and 34 (BHV). There is some indication, that the modelled PUR source is MDI-PUR which is highly source adherent. This has to be confirmed by further analysis and would probably require additional process description for MDI-PUR polymer in the model.

However, two significant points have to be made here: Despite huge efforts in sampling and lab analyses for MP loads the available data is still very limited and significantly more data would be necessary to allow a thorough calibration and have robust model results. Moreover, the need to convert particle numbers and averaged particle dimensions into MP mass introduces severe uncertainties as also discussed by Primpke et al. (2021).

The aforementioned points are the reason to consider this investigation merely as an exemplary showcase for the general feasibility of the presented type of model approach.

A model validation was done with a second and independent PLAWES data set. It is extracted from a larger data set (Halbach & Scholz-Böttcher, to be published elsewhere) and refers to respective polymer type clusters, each of which can be traced back to a base polymer type. The advantage of Py-GC/MS-results clearly is their direct measurement of MP masses, which makes the particle count to mass conversion step unnecessary and avoids the additional uncertainty introduced by the required assumptions (see also chapter 2.3.3.3). The presented dataset covers only the size fraction smaller 500 μm for selected sampling locations in and around the ETZ (Fig. 11).

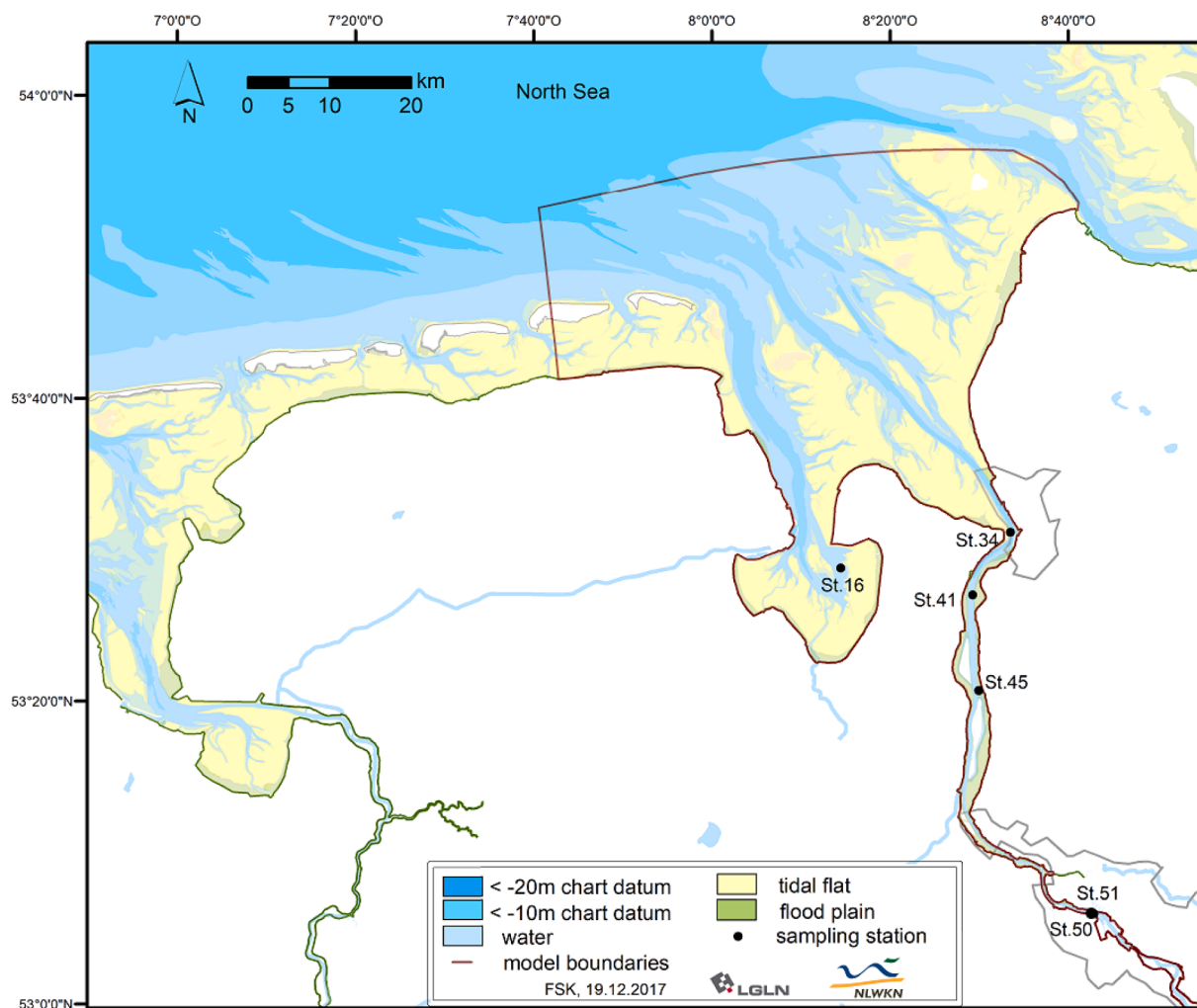In the light of the poor overall data density and the coarse calibration

Fig. 11. Measuring sampling stations for MP-mass concentration comparison with model results. (For interpretation of the references to colours in this figure, the reader is referred to the web version of this article.)

it makes no sense to further discuss the specific deviations between model and measurements here. Instead the reader should realize, that the model approach presented in this study allows very specific identification of existing data shortages with respect to location, MP polymer type, and physical process formulation.

Fig. 13 (a-h) shows 28-days averaged spatial distribution of the surface water MP concentration. Since the model distinguishes between several polymer types and size classes (Table 2) with different transport properties, the time averaged spatial distribution is shown separately for each polymer type.

The highest concentrations are generally found in and around the ETZ between BRK and BHV (locations see Fig. 6), which is in good agreement with the observations. As an example the distributions of PP and PC show significant differences regarding their time-averaged spatial distribution, because of their different physical properties and also their availability in the model (boundaries and sources): PC is significantly denser then PP, which lets PC-particles settle fast, while PP is negatively buoyant and is therefore dominantly transported in the upper water column, at least as biofouling in the outer estuary is weak and did not force the PP particles to settle. As an exemplary qualitative result one can assume, that PP particles easier leave the estuarine zone towards the open sea than PC particles do. It also becomes clear, that the ETZ strongly aggregates MP in the high concentrated mud suspension and bottom sediment, which serves as a MP sink with respect to the water body.

As PUR so far is modelled without any source adherence, the calculated spatial spreading might be far too strong.

Further need for improvement is given for the MP sources that contribute MP into the estuary. This for now applies to WWTPs and atmospheric deposition. On the one hand possibly relevant sources are not yet included (e.g. MP input from dewatering of the hinterland, tire wear) and on the other hand the available measurements from literature and also from PLAWES are more or less spot samples that had to be extended to larger time frames as well as a multitude of specific source locations. As the result of this investigation shows, this might already work as input for some general model runs, but definitely does not allows robust results, e.g. to base regulations or management options or assessments on them.

A comprehensive long-term monitoring program for MP-measurements is strongly envisaged. It could start for the tidal reach of the River Weser and be extended to other parts of the coastline, if necessary. It should include all WWTP effluents and dewatering inflows as well as atmospheric deposition along the Weser River. The main aim should be to elucidate the corresponding contribution of those sources. In parallel the transferability of this data to other estuaries should be checked.

In the light of the excessive efforts for sample analyses the combination of model results and targeted sampling and analysis seems as a promising approach to purposefully optimize sampling campaigns and also improve the system understanding by further model result
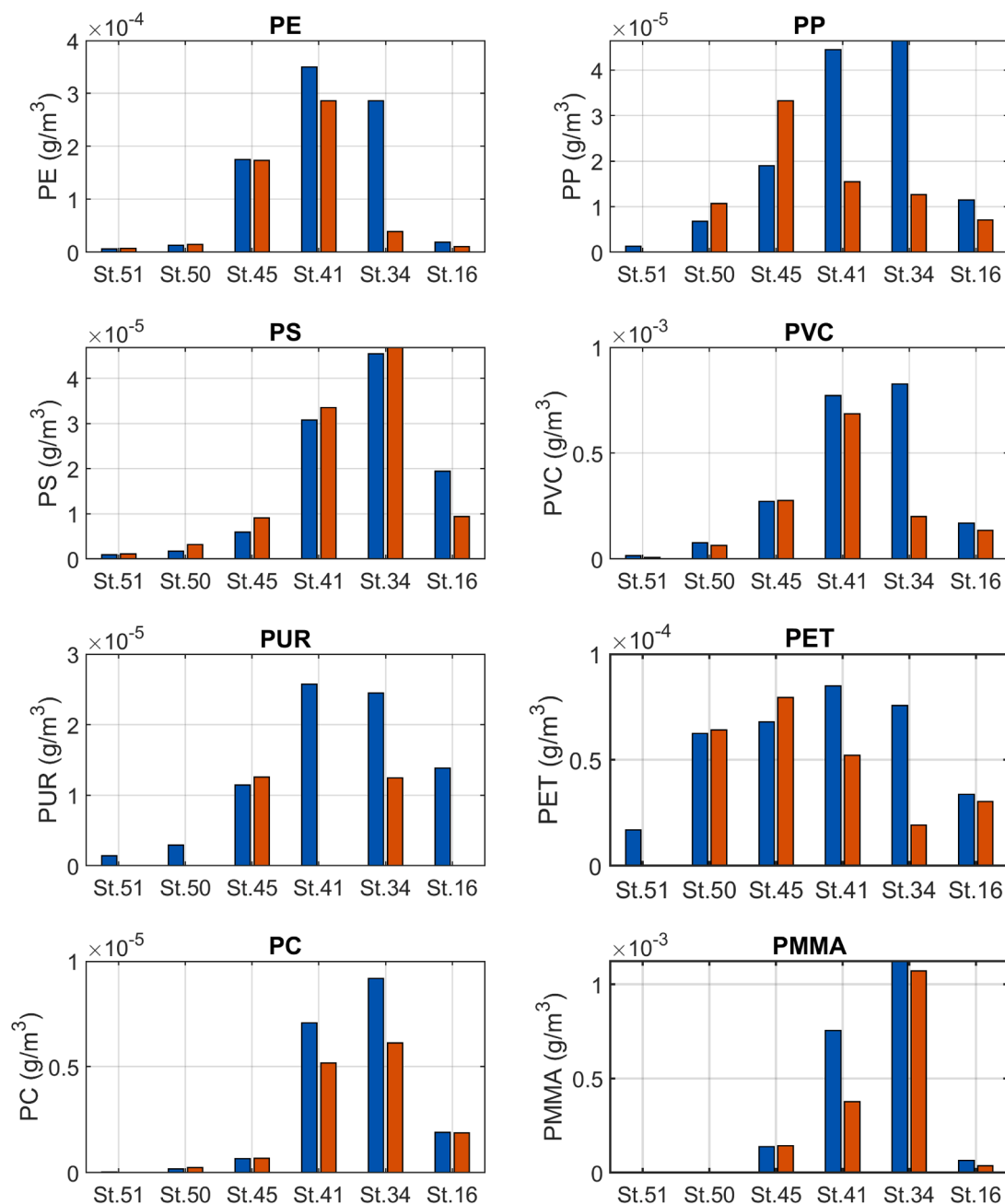
Fig. 12. Comparison between the MP concentration reproduced by model (blue columns) and measurements (red columns, equivalent to the respective mass of polymer clusters) by Py-GC/MS results for small MP(<500 μm). (For interpretation of the references to colours in this figure, the reader is referred to the web version of this article.)

validation. This mutual dependency should be considered for any further research of MP pollution on larger spatial scales.

4. Summary and conclusion

This paper presents a numerical model approach to study the transport and accumulation of MP in rivers. The hydrodynamic model formulation is suited for virtually all water bodies up to partially stratified estuaries. The paper shows an exemplary model application for the tidal influenced part of the River Weser and its estuary. Model development and application were carried out within the project framework of PLAWES, which covered the whole Weser catchment and dealt with MP sample analyses, modeling and other, mostly process based developments.

For the tidal region it was hypothesized, that MP to a certain extent would become part of the complex estuarine dynamics, especially the large scale baroclinic circulation and in term of interaction with suspended fine sediments, which accumulate in the estuarine turbidity zone and exhibit complex flocculation and hindered settling behavior. Therefore the MP transport model requires a fully coupled three-dimensional hydro- morphodynamic estuarine model as an important prerequisite. The MP transport also considers biofouling of MP particles, which also requires a simplified water quality model for micro algae. Since the presence of MP does by no means influence the hydro- and morphodynamic situation, the MP-transport model can be executed in a post-processing step after the hydro-morphodynamical model run.

The MP transport model is implemented based on convection-diffusion-type equations. It considers several MP-polymer types and

Table 3

Py-GC/MS mass concentration measurements and model results for sampling stations in Fig. 12.

(C-) PE(<500 μm)-concentration (g/m³)			(Statistical) Analysis		
Sampling station	Model results	PLAWES campaign (Py-GC/MS)	mean(Δ)	BSS	r (%)
St.51	$6.03 \times 10^{(-6)}$	$7.27 \times 10^{(-6)}$	$3.73 \times 10^{(-5)}$	0.42	67
St.50	$1.33 \times 10^{(-5)}$	$1.48 \times 10^{(-5)}$			
St.45	$1.75 \times 10^{(-4)}$	$1.73 \times 10^{(-4)}$			
St.41	$3.50 \times 10^{(-4)}$	$2.86 \times 10^{(-4)}$			
St.34	$2.86 \times 10^{(-4)}$	$3.90 \times 10^{(-5)}$			
St.16	$1.86 \times 10^{(-5)}$	$1.05 \times 10^{(-4)}$			

(C-)PP(<500 μm)- concentration (g/m³)			(Statistical) Analysis		
Sampling station	Model results	PLAWES campaign (Py-GC/MS)	mean(Δ)	BSS	r (%)
St.51	$1.33 \times 10^{(-6)}$	0.0	$8.39 \times 10^{(-6)}$	−0.33	33
St.50	$6.80 \times 10^{(-6)}$	$1.07 \times 10^{(-5)}$			
St.45	$1.90 \times 10^{(-5)}$	$3.32 \times 10^{(-5)}$			
St.41	$4.44 \times 10^{(-5)}$	$1.55 \times 10^{(-5)}$			
St.34	$4.65 \times 10^{(-5)}$	$1.26 \times 10^{(-5)}$			
St.16	$1.14 \times 10^{(-5)}$	$7.12 \times 10^{(-6)}$			

(C-)PS(<500 μm)- concentration (g/m³)			(Statistical) Analysis		
Sampling station	Model results	PLAWES campaign (Py-GC/MS)	mean(Δ)	BSS	r (%)
St.51	$9.22 \times 10^{(-7)}$	$1.14 \times 10^{(-6)}$	$1.87 \times 10^{(-7)}$	0.96	96
St.50	$1.73 \times 10^{(-6)}$	$3.17 \times 10^{(-6)}$			
St.45	$6.00 \times 10^{(-6)}$	$9.14 \times 10^{(-6)}$			
St.41	$3.08 \times 10^{(-5)}$	$3.36 \times 10^{(-5)}$			
St.34	$4.55 \times 10^{(-5)}$	$4.69 \times 10^{(-5)}$			
St.16	$1.95 \times 10^{(-5)}$	$9.38 \times 10^{(-6)}$			

(C-)PVC(<500 μm)- concentration (g/m³)			(Statistical) Analysis		
Sampling station	Model results	PLAWES campaign (Py-GC/MS)	mean(Δ)	BSS	r (%)
St.51	$1.50 \times 10^{(-5)}$	$7.01 \times 10^{(-6)}$	$1.02 \times 10^{(-4)}$	0.32	71
St.50	$7.57 \times 10^{(-5)}$	$6.48 \times 10^{(-5)}$			
St.45	$2.71 \times 10^{(-4)}$	$2.76 \times 10^{(-4)}$			
St.41	$7.73 \times 10^{(-4)}$	$6.86 \times 10^{(-4)}$			
St.34	$8.27 \times 10^{(-4)}$	$2.00 \times 10^{(-4)}$			
St.16	$1.69 \times 10^{(-5)}$	$1.35 \times 10^{(-4)}$			

(C-)MDI-PUR(<500 μm)- concentration (g/m³)			(Statistical) Analysis		
Sampling station	Model results	PLAWES campaign (Py-GC/MS)	mean(Δ)	BSS	r (%)
St.51	$1.41 \times 10^{(-6)}$	0.0	$9.15 \times 10^{(-6)}$	−2.25	35
St.50	$2.91 \times 10^{(-6)}$	0.0			
St.45	$1.15 \times 10^{(-5)}$	$1.26 \times 10^{(-5)}$			
St.41	$2.58 \times 10^{(-5)}$	0.0			
St.34	$2.45 \times 10^{(-5)}$	$1.24 \times 10^{(-5)}$			
St.16	$1.38 \times 10^{(-5)}$				

Table 3 (*continued*)

(C-) PE (<500 μm)-concentration (g/m³)			(Statistical) Analysis		
Sampling station	Model results	PLAWES campaign (Py-GC/MS)	mean(Δ)	BSS	r (%)

(C-)PET(<500 μm)- concentration (g/m³)			(Statistical) Analysis		
Sampling station	Model results	PLAWES campaign (Py-GC/MS)	mean(Δ)	BSS	r (%)
St.51	$1.69 \times 10^{(-5)}$	0.0	$1.60 \times 10^{(-5)}$	0.67	60
St.50	$6.24 \times 10^{(-5)}$	$6.42 \times 10^{(-5)}$			
St.45	$6.79 \times 10^{(-5)}$	$7.96 \times 10^{(-5)}$			
St.41	$8.50 \times 10^{(-5)}$	$5.22 \times 10^{(-5)}$			
St.34	$7.57 \times 10^{(-5)}$	$1.92 \times 10^{(-5)}$			
St.16	$3.37 \times 10^{(-5)}$	$3.03 \times 10^{(-5)}$			

(C-)PC(<500 μm)- concentration (g/m³)			(Statistical) Analysis		
Sampling station	Model results	PLAWES campaign (Py-GC/MS)	mean(Δ)	BSS	r (%)
St.51	$2.85 \times 10^{(-8)}$	0.0	$8.16 \times 10^{(-7)}$	0.81	99
St.50	$1.77 \times 10^{(-7)}$	$2.31 \times 10^{(-7)}$			
St.45	$6.70 \times 10^{(-7)}$	$6.90 \times 10^{(-7)}$			
St.41	$7.06 \times 10^{(-6)}$	$5.18 \times 10^{(-6)}$			
St.34	$9.17 \times 10^{(-6)}$	$6.13 \times 10^{(-6)}$			
St.16	$1.90 \times 10^{(-6)}$	$1.88 \times 10^{(-6)}$			

(C-)PMMA(<500 μm)- concentration (g/m³)			(Statistical) Analysis		
Sampling station	Model results	PLAWES campaign (Py-GC/MS)	mean(Δ)	BSS	r (%)
St.51	$1.24 \times 10^{(-6)}$	$2.34 \times 10^{(-7)}$	$7.57 \times 10^{(-5)}$	0.89	95
St.50	$2.78 \times 10^{(-6)}$	$3.86 \times 10^{(-6)}$			
St.45	$1.39 \times 10^{(-4)}$	$1.44 \times 10^{(-4)}$			
St.41	$7.56 \times 10^{(-4)}$	$3.77 \times 10^{(-4)}$			
St.34	$1.12 \times 10^{(-3)}$	$1.07 \times 10^{(-3)}$			
St.16	$6.59 \times 10^{(-5)}$	$3.57 \times 10^{(-5)}$			

their particle size classes. The deterministic approach includes interaction with the estuarine processes on different levels. The dominant governing process for the MP here is the settling velocity formulation, which considers MP particles as either inert or part of sediment aggregates, which form by means of flocculation and aggregation processes and also hindered settling. Also biofouling is included in terms of settling velocity formulation. Furthermore MP sedimentation, erosion and resuspension are considered.

To run the model initial and boundary conditions are needed and –as far as MP is concerned- this draws relevant constraints on the model application so far, since measured data are hardly available. Therefore, besides μFTIR data analyzed within PLAWES literature values had to be used to estimate initial and boundary conditions and additional MP sources.

The available data allowed a coarse calibration of the MP transport model which leads to good results that could also be validated by means of the first exemplary data of a more comprehensive Py-GC/MS dataset to be published elsewhere. The good overall agreement between model and data is a result of the strongly deterministic character of the MP binding to the estuarine processes. Nonetheless the sparse available input data renders the application shown here merely as an exemplary showcase for the general feasibility of the presented type of model
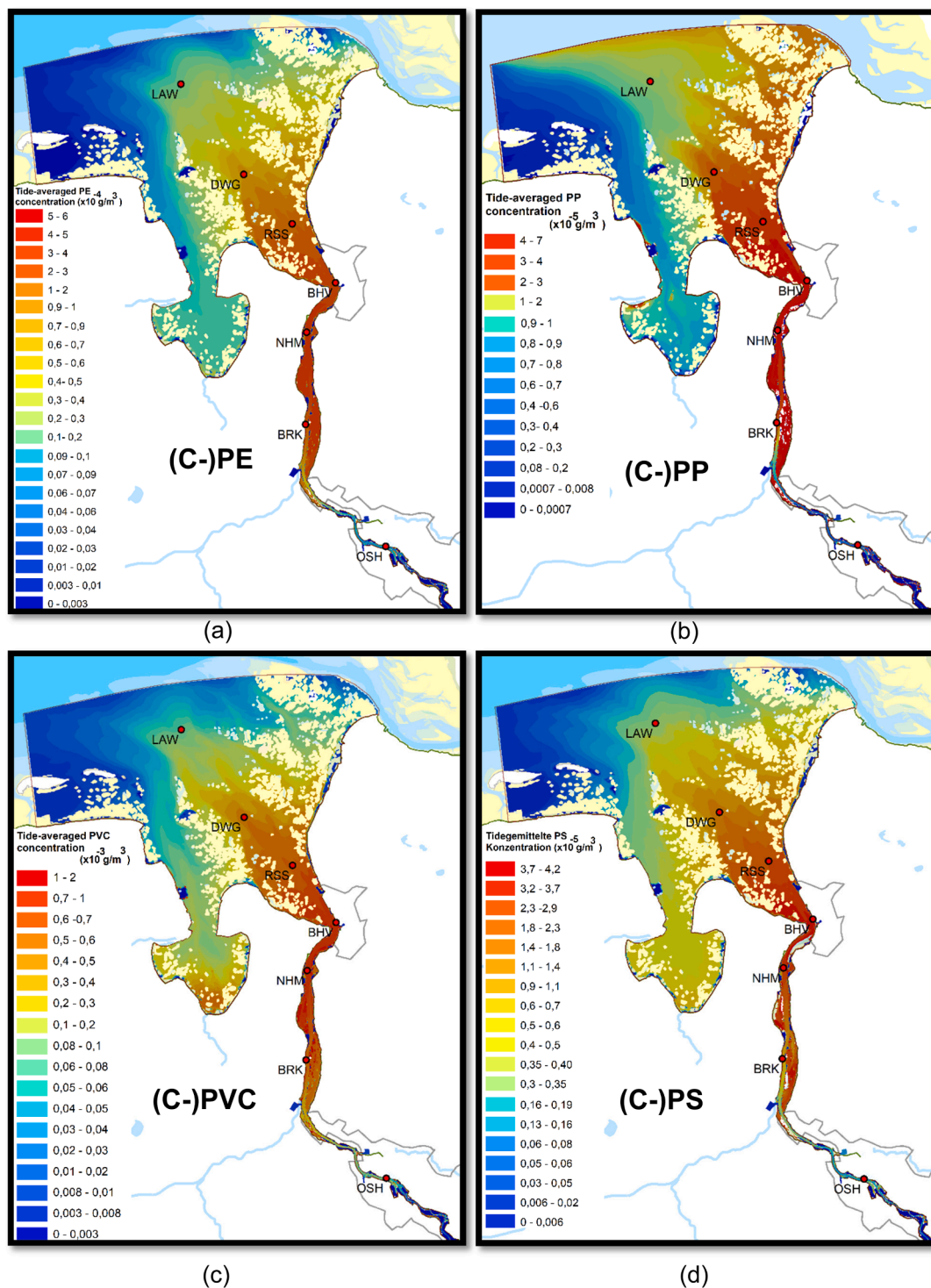
Fig. 13. (a-h). Time averaged MP-mass concentration (g/m³) in the water surface layer (<1 m) for small MP polymers (<500 μm). (For interpretation of the references to colours in this figure, the reader is referred to the web version of the article.)

approach.

The definite conclusion at the present time is, that the model can contribute to an efficient as well as organized campaign measurements. Therefore a combination of both provides much more progress than each of them separately.

The model approach is suited to consistently extend the point measurements into the complete model area and provides a powerful aid towards better system understanding. Also the model allows to increase

the representativeness of the point measurements, which can be considered as a spotlight within a significantly dynamic system, by means of time averaging the model results.

The results clearly show, that the combination of both, model application and improvement as well as targeted measurements provides much more progress for further improvement of system understanding compared to each of them separately. A suggestion for a long term monitoring and analysis program is given.
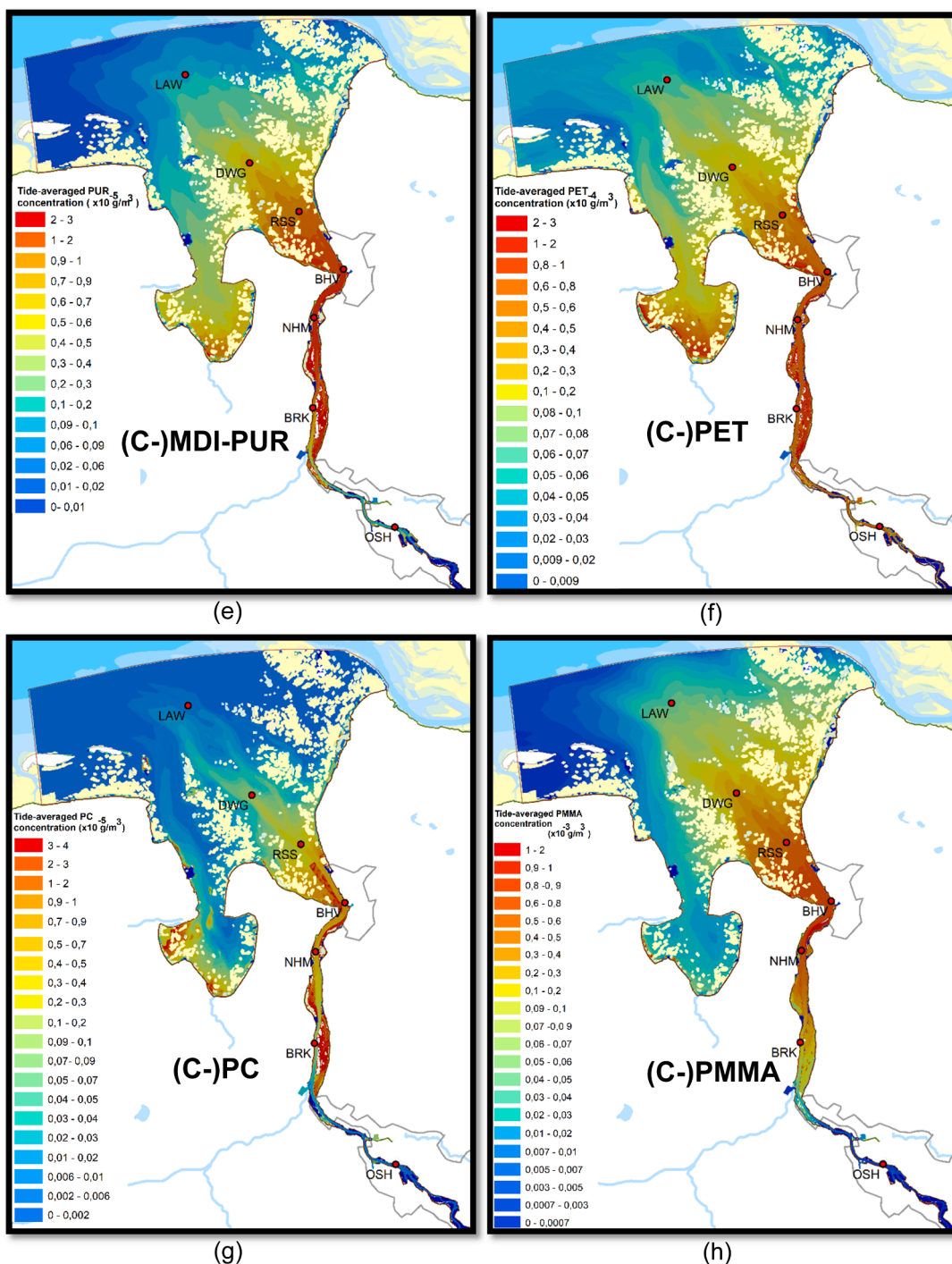
Fig. 13. (*continued*).

Declaration of Competing Interest

The authors declare that they have no known competing financial interests or personal relationships that could have appeared to influence the work reported in this paper.

Data availability

Data will be made available on request.

Supplementary materials

Supplementary material associated with this article can be found, in the online version, at doi:10.1016/j.watres.2022.119564.

References

Akoglu, H., 2018. User's guide to correlation coefficients. Turk. J. Emerg. Med. 18 (3), 91–93. https://doi.org/10.1016/j.tjem.2018.08.001.

Allen, S., Allen, D., Karbalaei, S., Maselli, V., Walker, T.R., 2022. Micro (nano) plastics sources, fate, and effects: what we know after ten years of research. J. Hazard. Mater. 6, 100057 https://doi.org/10.1016/j.hazadv.2022.100057.

Andersen, T.J., Rominikan, S., Olsen, I.S., Skinnebach, K.H., Fruergaard, M., 2021. Flocculation of PVC microplastic and fine-grained cohesive sediment at environmentally realistic concentrations. Biol. Bull. 240 (1), 42–51. https://doi.org/10.1086/712929.

Andrady, A.L., 2022. Weathering and fragmentation of plastic debris in the ocean environment. Mar. Pollut. Bull. 180, 113761 https://doi.org/10.1016/j.marpolbul.2022.113761.

Arthur, C., Baker, J.E., & Bamford, H.A. (2009). Proceedings of the International Research Workshop on the Occurrence, Effects, and Fate of Microplastic Marine Debris, September 9-11, 2008, University of Washington Tacoma, Tacoma, WA, USA.

Auta, H.S., Emenike, C.U., Fauziah, S.H., 2017. Distribution and importance of microplastics in the marine environment: a review of the sources, fate, effects, and potential solutions. Environ. Int. 102, 165–176. https://doi.org/10.1016/j.envint.2017.02.013.

Becker, M., Schrottke, K., Bartholomä, A., Ernstsen, V., Winter, C., Hebbeln, D., 2013. Formation and entrainment of fluid mud layers in troughs of subtidal dunes in an estuarine turbidity zone. J. Geophys. Res. 118 (4), 2175–2187. https://doi.org/10.1002/jgrc.20153.

Brandes, E., Cieplik, S., Fiener, P., Henseler, M., Herrmann, F., Klasmeier, J., Kreins, P., Piel, S., Shiravani, G., Wendland, F., & Wurpts, A. (2020). Modellbasierte Forschung zu Mikroplastik in der Umwelt. Modellbasierte Forschung zu Mikroplastik in der Umwelt | Plastik in der Umwelt (bmbf-plastik.de).

Enders, K., Käppler, A., Biniasch, O., Feldens, P., Stollberg, N., Lange, X., Fischer, D., Eichhorn, K.J., Pollehne, F., Obebeckmann, S., Labrenz, M., 2019. Tracing microplastics in aquatic environments based on sediment analogies. Sci. Rep. 9 (1), 1–15. https://doi.org/10.1038/s41598-019-50508-2.

Da Costa, J.P., Rocha-Santos, T., Duarte, A.C., 2020. The Environmental Impacts of Plastics and Micro-Plastics Use, Waste and Pollution: EU and National Measures. European Union. http://www.europarl.europa.eu/supporting-analyses.

Deltares. (2021a). Delft3D-FLOW, User Manual, 2021. Version 3.15, SVN Revision: 72836, Deltares, The Netherlands.

Deltares, 2021b. D-Water Quality, User Manual, 2021. Version 1.1, SVN Revision: 71974. Deltares, the Netherlands.

Dibke, C., Fischer, M., Scholz-Böttcher, B.M., 2021. Microplastic mass concentrations and distribution in German bight waters by pyrolysis–gas chromatography–mass spectrometry/thermochemolysis reveal potential impact of marine coatings: do ships leave skid marks? Environ. Sci. Technol. 55 (4), 2285–2295. https://doi.org/10.1021/acs.est.0c04522.

Dietrich, W.E., 1982. Settling velocity of natural particles. Water Resour. Res. 18 (6), 1615–1626. https://doi.org/10.1029/WR018i006p01615.

Fazey, F.M.C., Ryan, P.G., 2016. Biofouling on buoyant marine plastics: an experimental study into the effect of size on surface longevity. Environ. Pollut. 210, 354–360. https://doi.org/10.1016/j.envpol.2016.01.026.

Fredsoe, J., Deigaard, R., 1992. Mechanics of Coastal Sediment Transport (Vol. 3). World Scientific Publishing Company.

Fischer, M., Scholz-Böttcher, B.M., 2017. Simultaneous trace identification and quantification of common types of microplastics in environmental samples by pyrolysis-gas chromatography–mass spectrometry. Environ. Sci. Technol. 51 (9), 5052–5060. https://doi.org/10.1021/acs.est.6b06362.

Fischer, M., Scholz-Böttcher, B.M., 2019. Microplastics analysis in environmental samples–recent pyrolysis-gas chromatography-mass spectrometry method improvements to increase the reliability of mass-related data. Anal. Methods 11 (18), 2489–2497. https://doi.org/10.1039/C9AY00600A.

Geyer, R., Jambeck, J., R., Law, K.L., 2017. Production, use, and fate of all plastics ever made. Sci. Adv. 3 (7), 1–5. https://doi.org/10.1126/sciadv.1700782 e1700782.

Green, D.S., Boots, B., O'Connor, N.E., Thompson, R., 2017. Microplastics affect the ecological functioning of an important biogenic habitat. Environ. Sci. Technol. 51 (1), 68–77. https://doi.org/10.1021/acs.est.6b04496.

Hartsuiker, G., 2003. Tidal Model Weser Estuary. Alkyon Report A 589 (not published).

Jung, J.W., Kim, S., Kim, Y.S., Jeong, S., Lee, J., 2022. Tracing microplastics from raw water to drinking water treatment plants in Busan, South Korea. Sci. Total Environ. 825, 154015 https://doi.org/10.1016/j.scitotenv.2022.154015.

Kaiser, D., Kowalski, N., Waniek, J.J., 2017. Effects of biofouling on the sinking behavior of microplastics. Environ. Res. Lett. (12), 12. https://doi.org/10.1088/1748-9326/aa8e8b.

Kay, P., Hiscoe, R., Moberley, I., Bajic, L., McKenna, N., 2018. Wastewater treatment plants as a source of microplastics in river catchments. Environ. Sci. Pollut. Res. Int. 25 (20), 20264–20267. https://doi.org/10.1007/s11356-018-2070-7.

Kernchen, S., Löder, M.G., Fischer, F., Fischer, D., Moses, S.R., Georgi, C., Nölscher, A.C., Held, A., Laforsch, C., 2022. Airborne microplastic concentrations and deposition

across the Weser River catchment. Sci. Total Environ. 818, 151812 https://doi.org/10.1016/j.scitotenv.2021.151812.

Koelmans, B., Pahl, S., Backhaus, T., Bessa, F., van Calster, G., Contzen, N., Cronin, R., Galloway, T., Hart, A., Henderson, L., Kalčíková, G., Kelly, F., Kolodziejczyk, B., Marku, E., Poortinga, W., Rillig, M., van Sebille, E., Steg, L., Steinhorst, J., Steidl, J., Syberg, K., Thompson, R., Wagner, M., van Wezel, A., Wyles, K., Wright, S., 2019. SAPEA, Science Advice for Policy by European Academies (2019). A Scientific Perspective on Microplastics in Nature and Society. SAPEA, Berlin. https://doi.org/10.26356/microplastics.

Knaack, H., Kaiser, R., Hartsuiker, G., Mayerle, R., & Niemeyer, H.D. (2006). *Ermittlung der Bemessungswasserstände für die Unterweser mit mathematischen Modellen,* Forschungsbericht 01/06 NLWKN-Forschungsstelle Küste (not published).

Kooi, M., Koelmans, A.A., 2019. Simplifying microplastic via continuous probability distributions for size, shape, and density. Environ. Sci. Technol. Lett 6 (9), 551–557. https://doi.org/10.1021/acs.estlett.9b00379.

Kooi, M., van Nes, E.H., Scheffer, M., Koelmans, A.A., 2017. Ups and downs in the ocean: effects of biofouling on vertical transport of microplastics. Environ. Sci. Technol. 51 (14), 7963–7971. https://doi.org/10.1021/acs.est.6b04702.

Krone, R.B., 1962. Flume Studies of Transport of Sediment in Estrarial Shoaling Processes. Hydr. Engr. and Sanitary Engr. Res. Lab., Univ. of California. Final Report.

Lebreton, L., Van Der Zwet, J., Damsteeg, J.W., Slat, B., Andrady, A., Reisser, J., 2017. River plastic emissions to the world's oceans. Nat. Commun. 8 (1), 1–10. https://doi.org/10.1038/ncomms15611.

Li, Y., Wang, X., Fu, W., Xia, X., Liu, C., Min, J., Zhang, W., Crittenden, J.C., 2019. Interactions between nano/micro plastics and suspended sediment in water: implications on aggregation and settling. Water Res. 161, 486–495. https://doi.org/10.1016/j.watres.2019.06.018.

Laskar, N., Kumar, U., 2019. Plastics and microplastics: a threat to environment. Environ. Technol. Innov. 14, 100352 https://doi.org/10.1016/j.eti.2019.100352.

McCormick, M.I., Chivers, D.P., Ferrari, M.C., Blandford, M.I., Nanninga, G.B., Richardson, C., Fakan, E.P., Vamvounis, G., Gulizia, A.M., Allan, B.J., 2020. Microplastic exposure interacts with habitat degradation to affect behaviour and survival of juvenile fish in the field. Proc. R. Soc. B 287 (1937), 20201947. https://doi.org/10.1098/rspb.2020.1947.

Mengual, B., Le Hir, P., Cayocca, F., Garlan, T., 2017. Modelling fine sediment dynamics: towards a common erosion law for fine sand, mud and mixtures. Water 9 (8), 564. https://doi.org/10.3390/w9080564.

Mintenig, S.M., Kooi, M., Erich, M.W., Primpke, S., Redondo-Hasselerharm, P.E., Dekker, S.C., Koelmans, A.A., Van Wezel, A.P., 2020. A systems approach to understand microplastic occurrence and variability in Dutch riverine surface waters. Water Res. 176, 115723 https://doi.org/10.1016/j.watres.2020.115723.

Mintenig, S.M., Int-Veen, I., Löder, M.G.J., Primpke, S., Gerdts, G., 2017. Identification of microplastic in effluents of waste water treatment plants using focal plane array-based micro-Fourier-transform infrared imaging. Water Res. 108, 365–372. https://doi.org/10.1016/j.watres.2016.11.015.

Miri, S., Saini, R., Davoodi, S.M., Pulicharla, R., Brar, S.K., Magdouli, S., 2022. Biodegradation of microplastics: better late than never. Chemosphere 286, 131670. https://doi.org/10.1016/j.chemosphere.2021.131670.

Oberrecht, D., 2021. Development of a Numerical Modeling Approach for Large-Scale Fluid Mud Flow in Estuarine Environments. Gottfried Wilhelm Leibniz Universität, Hannover. https://doi.org/10.15488/10488. Diss., 2020, xvi, 118 S.

PlasticsEurope Association of Plastics Manufactures, 2020. Plastics the Facts 2020 an analysis of European plastics, production, demand and waste data. Plastics - the Facts 2020 • Plastics Europe.

Partheniades, E., 1965. Erosion and deposition of cohesive soils. Journal of the Hydraulics Division 91 (1), 105–139.

PlasticsEurope Association of Plastics Manufactures, 2009. The Compelling Facts About Plastics 2009 an analysis of European plastics, production, demand and recovery for 2008. 2009-Compelling-facts.pdf (plasticseurope.org).

Primpke, S., Fischer, M., Lorenz, C., Gerdts, G., Scholz-Böttcher, B.M., 2020. Comparison of pyrolysis gas chromatography/mass spectrometry and hyperspectral FTIR imaging spectroscopy for the analysis of microplastics. Anal. Bioanal. Chem. 412 (30), 8283–8298. https://doi.org/10.1007/s00216-020-02979-w.

Primpke, S., Booth, A.M., Gerdts, G., Gomiero, A., Kögel, T., Lusher, A.L., Strand, J., Scholz-Böttcher, B.M., Galgani, F., Provencher, J., Aliani, S., Patankar, S., Vorkamp, K., 2022. Monitoring of microplastic pollution in the Arctic: recent developments in polymer identification, quality assurance and control (QA/QC), and data reporting. Arc. Sci. https://doi.org/10.1139/as-2022-0006.

Roscher, L., Fehres, A., Reisel, L., Halbach, M., Scholz-Böttcher, B., Gerriets, M., Badewien, T.H., Shiravani, G., Wurpts, A., Primpke, S., Gerdts, G., 2021. Microplastic pollution in the Weser estuary and the German North Sea. Environ. Pollut. 288 https://doi.org/10.1016/j.envpol.2021.117681.

Ross, M.A., Mehta, A.J., 1989. On the mechanics of lutoclines and fluid mud. J. Coast. Res. 51–62. http://www.jstor.org/stable/25735365.

Ruggero, F., Gori, R., Lubello, C., 2020. Methodologies for microplastics recovery and identification in heterogeneous solid matrices: a review. J. Polym. Environ. 28 (3), 739–748. https://doi.org/10.1007/s10924-019-01644-3.

Schoellhamer, D.H., Ganju, N.K., Mineart, P.R., Lionberger, M.A., 2008. Sensitivity and spin-up times of cohesive sediment transport models used to simulate bathymetric change. Proc. Mar. Sci. 9, 463–475. https://doi.org/10.1016/S1568-2692(08)80033-2.

Sharqawy, M.H., John, H.L.V., Sayed, M.Z., 2010. The thermophysical properties of seawater: a review of existing correlation and data. Desal. Water Treat. 16, 354–380.

Song, J., Beule, L., Jongmans-Hochschulz, E., Wichels, A., Gerdts, G., 2022. The travelling particles: community dynamics of biofilms on microplastics transferred

along a salinity gradient. ISME Commun. 2 (1), 1–12. https://doi.org/10.1038/s43705-022-00117-4.

Song, Y.K., Hong, S.H., Jang, M., Han, G.M., Jung, S.W., Shim, W.J., 2017. Combined effects of UV exposure duration and mechanical abrasion on microplastic fragmentation by polymer type. Environ. Sci. Technol. 51 (8), 4368–4376. https://doi.org/10.1021/acs.est.6b06155.

Toorman, E.A., 1992. Modeling of Fluid Mud Flow and Consolidation. Katholieke Universiteit Leuven. PhD Thesis.

Turner, A., Holmes, L.A., 2015. Adsorption of trace metals by microplastic pellets in fresh water. Environ. Chem. 12 (5), 600–610. https://doi.org/10.1071/EN14143.

Valerius, J., Feldman, J., van Zoest, M., Milbrat, P., Zeiler, M., 2013. Documentation of Morphological Products from the AufMod Project Functional Seabed Model. Data format: Text files (CSV, XYZ.

Valerius, J., Kösters, F., Zeiler, M., 2015. Erfassung von Sandverteilungsmustern zur großräumigen Analyse der Sedimentdynamik auf dem Schelf der Deutschen Bucht. Bundesanstalt für Wasserbau, Karlsruhe, pp. 39–63. Die Küste 83.

Van Rijn, L.C., 1984. Sediment transport, part III: bed forms and alluvial roughness. J. Hydraul. Eng. 110 (12), 1733–1754. https://doi.org/10.1061/(ASCE)0733-9429(1984)110:12(1733).

Van Rijn, L.C., 1993. Principles of Sediment Transport in rivers, Estuaries and Coastal Seas. Vol. 1006. Aqua Publications, Amsterdam.

Van Rijn, L.C., Walstra, D.J., Grasmeijer, B., Sutherland, J., Pan, S., Sierra, J.P., 2003. The predictability of cross-shore bed evolution of sandy beaches at the time scale of storms and seasons using process-based profile models. Coast. Eng. 47 (3), 295–327. https://doi.org/10.1016/S0378-3839(02)00120-5.

Waldschläger, K., Schüttrumpf, H., 2019. Erosion behavior of different microplastic particles in comparison to natural sediments. Environ. Sci. Technol. https://doi.org/10.1021/acs.est.9b05394.

Wang, Z.T., Lai, Z.P., 2014. A theoretical model on the relation between wind speed and grain size in dust transportation and its paleoclimatic implications. Aeolian Res. 13, 105–108. https://doi.org/10.1016/j.aeolia.2014.04.003.

Wu, W., Perera, C., Smith, J., Sanchez, A., 2018. Critical shear stress for erosion of sand and mud mixtures. J. Hydraul. Res. 56 (1), 96–110. https://doi.org/10.1080/00221686.2017.1300195.